Status Report on Activities in Hall A - 1999

Edited by Edward J. Brash, Ronald D. Ransome, and Kees de Jager

January 1, 2000

Contents

1 The Facilities **8**

1.1 The Spectrometers (Contributed by J. Lerose) 8

1.1.1 General Properties 8

1.1.2 Future Developments 8

1.2 The Beamline (Contributed by A. Saha) 11

1.2.1 Absolute Energy Measurements 12

1.2.2 Current and Charge Calibrations 13

1.2.3 Beam Position and Direction 13

1.3 The Møller Polarimeter (Contributed by E. Chudakov) 15

1.3.1 Basics 15

1.3.2 General Description 15

1.3.3 Systematic Errors 16

1.3.4 Conclusion 16

1.4 The Compton Polarimeter (Contributed by M. Baylac) 17

1.4.1 Introduction 17

1.4.2 Commissionning 17

1.4.3 The Fabry-Pérot Cavity 18

1.4.4 First Evidence of Compton Events 19

1.4.5 Preliminary Results for HAPPEX 99 19

1.4.6 Skill Transferred to JLab Crew 20

1.5 The Polarized ^{3}He Target (Contributed by J.P Chen) 21

1.6 The Cryotarget (Contributed by M. Kuss) 24

1.7 Spectrometer Detector Package Development (Contributed by B. Wojtsekhowski) 26

1.7.1 Trigger Scintillators 26

1.7.2 Mirror Aerogel Detector (Contributed by J. Hovdebo) . . . 27

1.7.3 Diffusion Aerogel Cherenkov Counter 30

1.7.4 Diffusion Aerogel Cerenkov Counter Commissioning (Contributed by P. Markowitz) 31

1.7.5 Vertical Drift Chamber 34

1.7.6 Gas Cherenkov Counter 35

1.7.7 Pion rejector 36

1.7.8 Large Scintillator Arrays 36

1.7.9 Big Bite detector package 37

1.8 Data Acquisition and Trigger (Contributed by R.O. Michaels) . . . 38

1.9 Analysis Software (Contributed by J-O Hansen) 40

1.9.1 ESPACE 40

1.9.2 The Object-Oriented Analyzer 41

1.10 Optics Commissioning (Contributed by N. Liyanage) 43

1.10.1 Databases at 0.85 GeV/c 43

1.10.2 HRSe Databases above 3.0 GeV/c 43

1.10.3 Summary of available databases 43
1.10.4 Spectrometer constants calibration 44

2 Summaries of Experimental Activities 46
2.1 E89-003 46
2.2 E89-033 49
2.3 E91-026 51
2.4 E93-027 54
2.5 E94-010 56
2.6 E95-001 59
2.6.1 Introduction 59
2.6.2 Experiment 60
2.6.3 Expected Results 60
2.7 HAPPEX 62
2.8 E89-019, E94-102, E99-008 64
2.8.1 Status of the Experiment 64
2.9 E89-028 66
2.10 $K^+ \vec{\Lambda}^0$ 67
2.11 E99-114 71
2.11.1 Introduction 72
2.11.2 Proof of Mixed Beam Applicability 74
2.11.3 Layout of the Experiment 76

3 Members of the Hall A Collaboration 81

List of Figures

1 *Layout of the Compton polarimeter.* 18
2 *3D view of the optics table with the monolithic cavity.* 19
3 *Counting rate as a function of the vertical position of the electron beam inside the cavity.* 20
4 *Experimental asymmetry for right (R) and left (L) photon polarization.* 20
5 *ADC spectrum for signal (black) and background (grey).* 21
6 *Absolute value of the electron beam polarization as a function of time for HAPPEX data taken in May 1999. Errors are statistical only.* 22
7 *Absolute value of the electron beam polarization as a function of time for HAPPEX data taken in July 1999. Errors are statistical only.* 23
8 *Beta vs X position (in meters) on HA.* 26
9 *ADC spectrum for a single photomultiplier fit with a Gaussian background and 4 Gaussians to represent photoelectron peaks.* 27

10 *Sample quadratic correction to linearize ADC response.* 28
11 *ADC sum spectrum fit with Poisson distributions assuming different numbers of most probable number of photoelectrons: (a) Peak=5,* $\mu = 5.3$, *(b) Peak=6,* $\mu = 6.3$, *(c) Peak=7,* $\mu = 7.3$ 30
12 *Aerogel installation inside the dry tent.* 31
13 *The efficiency for* β*=1 and* β*=0.9 particles in the a) 3cm aerogel and b) 9 cm aerogel.* 33
14 *The (e,e'K) missing mass spectrum a) without and b) with a cut on the pulse height in the aerogel detector.* 34
15 *VDC time-to-distance conversion.* 35
16 *Pion Rejector counter.* 36
17 *Pion Rejector Amplitudes* 37
18 *Pion Rejector Acceptance.* 38
19 *Anode currents in 7x11 package.* 39
20 *Measured* $^{16}O(e,e'p)$ *missing energy spectrum for* $E_{beam} = 2.4$ *GeV at* $P_{miss} = 60$ *MeV/c.* 47
21 *Measured cross sections and DWIA calculations at* $E_{\rm beam}$ *= 2.4 GeV. The solid line is the Udias* et al. *calculation [10], and the dashed line is the Kelly calculation [11]. The* $1p_{1/2}$ *state cross section and calculations have been multiplied by a factor of 20.* . . . 48
22 *Measured left-right asymmetry* A_{LT} *and DWIA calculations at* $E_{\rm beam}$ *= 2.4 GeV* 49
23 *Cross sections measured at different missing momenta as a function of missing energy. The curves show the* $1s_{1/2}$*-state single-particle strength calculated by Kelly folded with the Lorentzian parameterization of Mahaux.* 50
24 *The separated response functions and the difference of the longitudinal and transverse spectral functions for the* $|\theta_{pq}| = 0^\circ$ *setting (*$\langle P_{miss}\rangle \approx$ *60 MeV/c). The calculations have been binned in the same manner as the data.* 51
25 *The deuteron elastic structure function* $A(Q^2)$ *from JLab experiment E91-026 compared to RIA and RIA+MEC theoretical calculations. Also shown are previous SLAC data.* 52
26 *The deuteron form factor* $F_d(Q^2)$ *times* $(Q^2)^5$ *(top) and the reduced deuteron form factor* $f_d(Q^2)$ *(bottom) from JLab E91-026 and from SLAC. The curve is the asymptotic pQCD prediction arbitrarily normalized to the data at* $Q^2 = 4$ *(GeV/c)*^{2}. 53
27 *JLab E91-026 preliminary results for the deuteron* $B(Q^2)$ *compared to RIA and RIA+MEC theoretical calculations (curves are as in Fig. 25). Also shown are previous Saclay, Bonn, and SLAC data.* 54

28 *(a) The ratio $\mu_p G_{Ep}/G_{Mp}$ from this experiment, compared with theoretical calculations; the absolute value of σ_{sys} is shown by the shaded area. (b) The ratio $Q^2 F_{2p}/F_{1p}$ for the same data, compared to the same theoretical models as in 3a and world data; symbols are [23](Upward Triangles),[24](Boxes),[25](Left Triangles), [26](Circles),[27](Right Triangles), [28](Diamonds), [29](Asterisks), and [30](Downward Triangles).* 56
29 *The neutron magnetic form factor G_M^n in units of the standard dipole parameterization, $\mu_n G_D$, in the low Q^2 region, as determined in recent measurements: Markowitz et al. [32] (open diamonds) using $d(e,e'n)$; Bruins et al. [33] (squares) and Anklin et al. [34] (triangle and solid diamonds) using the ratio $d(e,e'n)/d(e,e'p)$; and Gao et al. [35] (circle) using $^3\vec{\mathrm{He}}(\vec{e},e')$. The expected precision of E95-001 is shown as error bars marked by crosses.* 60
30 *Raw asymmetries for sequential data sets. Odd numbered sets have a negative sign due to the insertion of the half-wave plate.* 63
31 *Cross section for K^+ production compared to previous data and existing theories.* 69
32 *Longitudinal Λ^0 polarization.* 71
33 *Ratio of the RCS cross section to KN for $-t$=5 GeV^2 as a function of s. The points show expected data for E99-114.* 73
34 *Scaling of the RCS cross section as a function of θ_{cm}. The full circles are the Cornell data. The open circles represent the projected precision from our project. For the pQCD mechanism $n \equiv 6$* 73
35 *Longitudinal polarization transfer parameter A_{LL} at 4 GeV. The solid curve is the prediction based on the handbag mechanism. The other curves are pQCD calculations with various DA's. The point shows the planned datum with its error bar.* 74
36 *Counting rate in the calorimeter at one of RCS kinematics.* 74
37 *Projections of the $\Delta\theta$ versus $\Delta\phi$ plot onto the $\Delta\phi$ axis for the endpoint runs. The cuts for the different panels are discussed in the text.* 75
38 *Projections of the $\Delta\theta$ versus $\Delta\phi$ plot onto the $\Delta\phi$ axis for the off-endpoint runs. The cuts for the different panels are discussed in the text.* 75
39 *Schematic view of the RCS Photon Arm detectors.* 76
40 *Some results of shower parameters reconstruction, obtained by using calorimeter prototype 5×5 during test runs: a) – Normalized energy distribution, giving the energy resolution $\sigma = 4.6\%$ for 2.3 GeV electron. b) – Spatial resolution, obtained from the MWPC track and reconstructed shower cluster center, is $\sigma = 4.3$ mm for 2 GeV electron. c) – Energy deposition in adjacent modules, when 2 GeV electron hits the center of cluster. Portions of energy deposition in each module are given in percents.* . . . 78

List of Tables

1 *Quadrupole Properties* 8
2 *Useful Web Links* 9
3 *Expected Spectrometer Performance with Septum* 9
4 *Determination of Beam Parameters* 11
5 *Summary of Beam Energy measurements* 12
6 *BCM calibration coefficients, April, 1999* 13
7 *Coefficients for charge determination, April, 1999* 13
8 *BPM/harp calibration offsets (GEOFFS)* 14
9 *Systematic errors. The dilution factor presents the factor used to divide the raw asymmetry in order to obtain the polarization, if such a correction is done. The last line presents the sum of the errors in quadratures.* 16
10 *Nominal working temperatures and pressures. The resulting densities are also listed.* 24
11 *Spectrometer Database Summary.* 43
12 Γ_{HRSh} 45
13 Γ_{HRSe} 45
14 *Experimental Kinematics* 48
15 *The ratios* $\mu_p G_{Ep}/G_{Mp}$ *from this experiment.* 55
16 Λ^0 *polarization measured for radiator in and radiator out runs. Results are extracted for whole and half decay cone.* 70

List of Publications

http://www.jlab.org/Hall-A/publications/Talks/Lists/Publicationlist.html

Disclaimer

The status reports to follow are outlines intended to demonstrate the extent of the scientific activity in Hall A at Jefferson Lab during the past year. These outlines are **not** publications, and often contain preliminary results not intended, or not yet ready, for publication. Material from these reports should not be reproduced, represented, or quoted without permission from the authors and/or spokespersons.

1 The Facilities

1.1 The Spectrometers (Contributed by J. Lerose)

1.1.1 General Properties

The "High Resolution Spectrometers" (HRS) are a pair of optically identical magnetic spectrometers consisting of four magnets each. The configuration is Q1, Q2, Dipole, Q3, where the quadrupoles (Qi's) are superconducting $\cos(2\phi)$ magnets with a cylindrical iron collar. The Q1's differ from the Q2/3's in that they are shorter with a smaller aperture radius (see Table 1 for details[1]). The dipoles are 6.6 m long conical magnets with a field index, n=-1.25, and were designed to provide a 45° bend for central momenta up to 4 GeV/c [2]. These two spectrometers are nominally referred to as the Electron (HRSe) and Hadron (HRSh) Arms.

	Inner Radius	Overall Length	Effective Length	Gradient @ 4 GeV/c
Q1	0.15 m	1.86 m	0.941 m	7.785 T/m
Q2	0.30 m	2.98 m	1.827 m	3.087 T/m
Q3	0.30 m	2.98 m	1.827 m	2.856 T/m

Table 1: *Quadrupole Properties*

The HRS pair is designed to provide momentum resolution (δp/p) of 1x10^{-4} or better. To date, δp's of about 3x10^{-4} have been achieved. Incident beam energy spread and target multiple scattering easily account for the departure from the design specifications. Various spectrometer properties, including transfer functions for use in spectrometer simulations, preliminary acceptance studies, and collimator locations can be found on various links from the Hall A homepage (see Table 2).

1.1.2 Future Developments

Various spectrometer improvements presently in the works include:

- Absolute Calibration: Data were taken in September 1999 (elastic scattering on ^{12}C with measured beam energy) in order to determine the absolute calibration of the spectrometers with much greater accuracy than was previously possible. That data is being analyzed as of this writing. The expected accuracy will be at the few times 10^{-4} level.

- Q2/3 DAC's: Higher precision DAC's for use in the regulation of the Q2/3 power supplies have been developed and tested. These will be installed in

[1] Effective lengths given are those measured using a set of rotating coils on the Electron Arm magnets. See "Field Mapping of the Hall A High Resolution Spectrometers of the Thomas Jefferson National Accelerator Facility", submitted for publication to NIM, July 1999.

[2] Due to a resistive short in one of its coils the Hadron Dipole is limited to 3.25 GeV/c.

Hall A Homepage: http://www.jlab.org/Hall-A
Transfer functions for acceptance studies and Monte Carlo simulations: http://www.jlab.org/Hall-A/news/minutes/tranferfuncs.html
Collimator positioning information: http://www.jlab.org/Hall-A/news/minutes/collimator-distance.html
Calculated 1st Order Matrices: http://www.jlab.org/Hall-A/news/minutes/fo-matrix.html
General Spectrometer Characteristics: http://www.jlab.org/Hall-A/equipment/high-resol.html

Table 2: *Useful Web Links*

the next few months. The higher precision DAC's will provide more stable current output from the power supplies which will enhance the intrinsic resolution capabilities of the spectrometers.

- Positioning: Ongoing improvements are being made in the vertical postioning, horizontal positioning, and hydrostatic leveling systems.
- Septum Magnets: A pair of septum magnets is being designed and built by BWX Technologies (BWXT) of Lynchburg, Virginia under contract with INFN in Rome. These magnets, when installed on the front end of the HRS pair, will allow access to central scattering angles between 6° and 12.5° for each arm at central momentum up to 4 GeV/c [3].

Central Momenta	4 GeV/c
Horizontal Acceptance (19mrad = beamline side)	-19 mrad $< \phi <$ 24 mrad
Vertical Acceptance	-54 mrad $< \theta <$ 54 mrad
Minimum Central Scattering Angle	6°
Maximum Central Scattering Angle	12.5°
Momentum Resolution ($\sigma(\delta p/p)$) @ 2 GeV/c)	$<1\text{x}10^{-4}$ (varies with δ)
Vertical Angular Resolution (σ @ 2 GeV/c)	$<$ 1.0 mrad (varies with δ)
Horizontal Angular Resolution (σ @ 2 GeV/c)	$<$ 0.7 mrad (varies with δ)

Table 3: *Expected Spectrometer Performance with Septum*

The schedule for the septum program is as follows:

[3] Since the use of the septum magnet requires shifting the target position 80 cm upstream, it will NOT be possible to use a septum on one arm and not the other, i.e., both arms must be at 12.5° or less.

- January 2000: Final design review
- February 2000: Readiness review for E94-107 (1st septum experiment)
- July 2000: Delivery of 1st magnet at JLab
- September 2000: Delivery of 2nd magnet
- Summer-Fall 2000: Acceptance testing of magnets
- February 2001: Installation of septum magnets
- April 2001: Start data taking for E94-107

1.2 The Beamline (Contributed by A. Saha)

The control and measurement equipment along the beamline consists of various elements necessary to transport beam with the required specifications to the reaction target and the dump and to simultaneously measure the properties of the beam relevant to the successful implementation of the physics program. The resolution and accuracy requirements are such that special attention is paid to the following:

1. Determination of the beam energy
2. Control of the beam position, transverse emittance and stability.
3. Determination of the beam current, total charge, and polarization.

Parameter	Method		Accuracy	Comments
Energy	ARC	Absolute	2×10^{-4}	Invasive
			5×10^{-4}	Non-Invasive
		Relative	$\pm 1 \times 10^{-4}$	Non-Invasive
	eP	Absolute	2×10^{-4}	Invasive
Energy Width	OTR $\star$		$\frac{\Delta E}{E}(\sigma) \sim 1 \times 10^{-5}$	Non-Invasive
Current ($\geq 0.5\mu A$)	2 RF Cavities	Absolute	$\leq 2 \times 10^{-3}$	Non-Invasive
Charge ($\geq 0.5\mu A$)	2 RF Cavities	Absolute	$\leq 2 \times 10^{-3}$	Non-Invasive
Position (at Target)	2 BPM/Harp	Absolute	$140\mu m$	x,y online
Direction (at Target)	2 BPM/Harp	Absolute	$30\mu rad$	θ, ϕ online
Stability (at Target)	Fast Feedback $\star$		$\leq$ 720 Hz motion	
	Position		$\leq 20\mu m(\sigma)$	
	Energy		$\leq 1 \times 10^{-5}(\sigma)$	
Polarization	Møller	Absolute	$\frac{\Delta P}{P} \approx 3\%(\Rightarrow 2\%)$	Invasive
	Compton $\star$	Absolute	$(\frac{\Delta P}{P} \Rightarrow 2\%)$	Non-invasive

$\star$ Still under Development

Table 4: *Determination of Beam Parameters*

Table 4 lists all of the beam parameters monitored along the beamline and the requisite instrumentation. In nearly all cases, we have two or more independent methods to determine and monitor the various parameters, both to gain confidence in the absolute measurements and to have enough redundancy in the system if any of the instrumentation should fail during a run. The various elements along the beamline are already listed and described in the Operational Manual. As seen in Table 4, we determine and monitor the absolute values of the beam parameters at a level which in most cases meets or exceeds the needs of many of the approved experiments.

1.2.1 Absolute Energy Measurements

We have systematically started making beam energy measurements both with the Arc-Energy method and the eP method. The Arc method uses instrumentation in the arc section (Scanners, BdL measurements of the arc dipoles, etc.) developed initially by the French collaboration (Pascal Vernin and the Saclay group). The eP method was developed by the Clermont-Ferrand group (Pierre Bertin et al.) and is a stand-alone device along the beamline located 17 m upstreamof the target. Since October 1998, the absolute energy of the beam has been measured several times by both methods. These are listed and described in the electronic logbook.

The Arc-Energy method has consistently determined the beam energy with an absolute uncertainty of $\simeq 2 \times 10^{-4}$ (as designed) over this time period. With better understanding of the system and the residual magnetic field strengths along the arc section, we are able to understand the systematics to nearly a factor of two better. The eP-method has made significant progress in this same time period and is also approaching the same level of uncertainty in their systematics as the Arc-Energy method. In Table 5, we list the measurements where both methods have been performed together optimally (i.e., when the eP has been run with both arms).

We have greatly improved the beam optics tuning through the arc section into the hall. We have degaussed and deactivated all the beam correctors, sextupoles and all other extraneous magnetic elements in the arc section. We also maintain the same dipole field strength in the arc section between the regular achromatic and energy measuring dispersive tunes of the beam. This enables us to track and maintain the knowledge of the energy of the beam throughout the whole running period non-invasively. By not using the correctors and other magnetic elements within the arc section, we are also able to deliver a more stable and clean beam to the hall. We were able to demonstrate all this during the first part of the HAPPEX2 experiment (April - May 99), where we were able to measure and control the energy at 3355 MeV.

Date	Pass	ARC (MeV)	eP (MeV)
Oct 24, 98	4 Pass	3385 ± 0.6	3384 ± 1
Nov 6, 98	5 Pass	4236.2 ± 0.8	4240 ± 3
April 23, 99	3 Pass	3355.2 ± 0.7	3354.4 ± 0.7
May 29, 99	3 Pass	3355.1 ± 0.7	3355.0 ± 0.7
Sept 22, 99	2 Pass	1266.1 ± 0.4	1266.9 ± 0.5

Table 5: *Summary of Beam Energy measurements*

1.2.2 Current and Charge Calibrations

The beam current monitor (BCM) is designed for a stable, low noise, non-intercepting beam current measurement. It consists of an Unser monitor, two RF cavities, the electronics and a data acquisition system and is described in detail in the Operational Manual. The cavities and the Unser monitor are enclosed in a box to improve magnetic shielding and temperature stabilization. The box is located 25 m upstream of the target. In addition to the Unser monitor, we have also incorporated the use of the OLO2 cavity monitor and the Faraday cup 2 at the injector section to provide an absolute reference during calibration runs. We are therefore able to provide absolute current and total charge values for any run down to 0.5 μA with high accuracy. Several comprehensive and detailed calibration and linearity runs were performed since October 1998, and the results are posted in the logbook. The latest results are listed in Tables 6 and 7 (details are posted in HALOG Nos. 16690 and 16689).

Cavity	Coefficient
Upstream cavity	76.963
Downstream cavity	77.149

Table 6: *BCM calibration coefficients, April, 1999*

Current Ranges (μA)	U x 1	D x 1	U x 3	D x 3	U x 10	D x 10
$\geq$ 40	1348	1341	(4139)	(4141)		
0.5 - 100	1348	1341	4139	4141		
0.2 - 50					12552	13081

Table 7: *Coefficients for charge determination, April, 1999*

1.2.3 Beam Position and Direction

To determine the position and the direction of the beam on the experimental target point, two beam position monitors (BPMs) are located at distances 7.524 m (IPM1H03A) and 1.286 m (IPM1H03B) upstream of the target position. The standard difference-over-sum technique is then used to determine the relative position of the beam to within 100 μm for currents above 1 μA. The absolute position of the beam can be determined from the BPMs by calibrating them with respect to wire scanners (superharps) which are located adjacent to each of the BPMs (IHA1H03A at 7.353 m and IHA1H03B at 1.122 m upstream of the target). The wire scanners are surveyed absolutely with respect to the hall coordinates. Ta-

ble 8 shows the results of several separate calibration runs to relate the absolute positions for the beam as determined from the scanners and the BPMs.

The scanners have been surveyed several times and at present the results disagree with respect to each other at the level of 300 μm. We are trying to understand these differences and seeing whether we are able to absolutely survey these scanners to better than 100 μm.

BPM	Offset (μA)
IPM1H03Ax	345
IPM1H03Ay	365
IPM1H03Bx	-220
IPM1H03By	900

Table 8: *BPM/harp calibration offsets (GEOFFS)*

1.3 The Møller Polarimeter (Contributed by E. Chudakov)

1.3.1 Basics

The beam line is equipped with a Møller polarimeter, whose purpose is to measure the polarization of the electron beam delivered to the hall. The polarimeter exploits the process of Møller scattering $\vec{e}^- + \vec{e}^- \rightarrow e^- + e^-$. Its cross section depends on the beam and target polarizations $\mathcal{P}_{beam}$ and $\mathcal{P}_{target}$ as:

$$\sigma \propto (1 + \sum_{i=X,Y,Z} (A_{ii} \cdot \mathcal{P}_{targ\ i} \cdot \mathcal{P}_{beam\ i})), \tag{1}$$

where $i = X, Y, Z$ defines the projections of the polarizations. The analyzing power A depends on the scattering angle in the CM frame θ_{CM}. Assuming that the beam direction is along the Z-axis and that the scattering occurs in the ZX plane:

$$A_{ZZ} = -\frac{\sin^2\theta_{CM} \cdot (7 + \cos^2\theta_{CM})}{(3 + \cos^2\theta_{CM})^2}, A_{XX} = -\frac{\sin^4\theta_{CM}}{(3 + \cos^2\theta_{CM})^2}, A_{YY} = -A_{XX} \tag{2}$$

At $\theta_{CM} = 90°$ the analyzing power has its maximum $A_{ZZ\ max} = 7/9$. A transverse polarization also leads to an asymmetry, though the analyzing power is lower: $A_{XX\ max} = A_{ZZ}/7$. The main purpose of the polarimeter is to measure the longitudinal component of the beam polarization.

1.3.2 General Description

The Møller polarimeter uses ferromagnetic foils, magnetized in a magnetic field of about 300 G along their plane, as the polarized electron target. The target foils can be tilted at various angles to the beam in the horizontal plane, therefore the target polarization has both longitudinal and horizontal components. The spin of the incoming electron beam may have a horizontal component due to precession. In order to cancel out the horizontal component the polarization measurements are taken at two target angles of about 20° and 160° and the average was taken, since the horizontal contribution have opposite signs for these target angles. Additionally, this method reduces the impact of uncertainties in the target angle measurements. The target polarization was derived from the foil magnetization measurements. For the supermendur foil used in 1998-1999 a polarization of 7.60±0.23% was obtained. At a given target angle two sets of measurements with opposite directions of the target polarization are taken. Averaging the results helps to cancel some false asymmetries, for example the helicity driven asymmetry of the beam flux.

The Møller scattering events are detected with the help of a magnetic spectrometer consisting of three quadrupole magnets and a dipole magnet, which deflects the electron pairs scattered in a kinematic range of about $75° < \theta_{CM} < 105°$ and

$-5^\circ < \phi_{CM} < 5^\circ$ towards a detector. The detector consists of lead–glass calorimeter modules, split into two arms in order to detect the scattered and recoiling electrons in coincidence. The beam helicity driven asymmetry of the coincidence counting rate (typically about 10^5/sec) is used to derive the beam polarization. In addition to detecting the counting rates, about 300/sec of "minimum bias" events containing the amplitudes and timings of all signals involved are recorded with a soft trigger from one arm. These data are used for various checks and tuning, and also for studying the non–Møller background.

A typical Møller measurement takes about 1 h plus typically about 40 min for setting and resetting the magnets. The statistical error for such a measurement is about 0.5% relative.

1.3.3 Systematic Errors

The systematic errors are presented in Table 9.

Origin	Dilution factor	Relative error
Target polarization	0.076	3.0%
Target angle	0.94	0.5%
Analyzing power	0.76	0.3%
Transverse polarization	-	0.3%
non-polarized background	-	<1.0%
dead-time	-	1.0%
observed fluctuations	-	1.0%
		3.5%

Table 9: *Systematic errors. The dilution factor presents the factor used to divide the raw asymmetry in order to obtain the polarization, if such a correction is done. The last line presents the sum of the errors in quadratures.*

1.3.4 Conclusion

Between Oct. 1, 1998 and Sept. 30, 1999, 79 measurements of the beam polarization were made. The systematic error of each measurement is estimated to be about 3.5% relative, while the statistical error is about 0.5%.

New studies of the systematic errors are planned. There is a hope to reduce the full systematic error to about 3%. A new set of quadrupole magnets will be installed downstream of the Møller polarimeter in January, 2000. This should help providing common magnet settings for the Møller measurements and the regular running, reducing the overhead time.

1.4 The Compton Polarimeter (Contributed by M. Baylac)

1.4.1 Introduction

The Compton polarimeter aims to determine the polarization of the electron beam delivered. It was designed to measure the polarization concurrently with experiments running in the hall to 1% statistical error within an hour. This project was realized by a collaboration between Saclay (France), Jefferson Laboratory, and the LPC Clermont-Ferrand (France). The polarization is extracted from the measurement of the counting rate asymmetry for opposite electron helicities in the scattering of a circularly polarized photon beam off the electron beam.

Installed in the entrance of the hall, the Compton polarimeter consists of a magnetic chicane, a photon source, an electromagnetic calorimeter, and an electron detector as shown in Fig. 1.

A fast front-end electronics and acquisition system is required to treat data up to 100 kHz.

The electron beam is deflected vertically by the 4 dipoles of the chicane and crosses the photon beam at the Compton interaction point (CIP). After interaction, the backscattered photons are detected in the calorimeter and the electrons in the silicon strip electron detector. Electrons that did not interact exit the polarimeter without perturbation and reach the target.

1.4.2 Commissionning

The first version of the polarimeter was installed between January and March, 1998 by Saclay and JLab people. The setup consisted of the 4 dipoles, the beam line, the vacuum system as well as the photon detector, the electronics and a 700 mW laser. The chicane was commissioned early March and we showed that the electron beam (up to 100 μA) goes through the chicane without any perturbation downstream.

We were unable to detect a clear evidence of a Compton signal during 1998. Indeed, the background rate recorded in the photon detector was abnormally high: more than 100 kHz at 100 μA. It was determined that the background was due to a beam halo interacting with mirror holders located 5 mm away from the electron beam. This halo was also seen in Hall B. Many investigative studies of the beam tuning were performed with the accelerator people (bunch length reduction, Lambertson steering, etc.) but were unsuccessful in substantially reducing the background.

In February 1999, an optical cavity (Section 1.4.3) was installed in the polarimeter to enhance the Compton luminosity. In addition we were able to isolate the parameter that mainly affected the background, i.e., the beam focusing in the chicane. We were able to reduce the background rate by a factor of 1000. Beam tuning inside the hall remains a delicate issue because focusing has to be done for both the Compton polarimeter and the target.

1.4.3 The Fabry-Pérot Cavity

The resonant Fabry-Pérot cavity is used as a power buildup for the photon beam. This monolithic cavity, 85 cm long, uses 2 high finesse mirrors ($\mathcal{F}$=26000) to amplify a primary 300 mW CW Nd:YaG laser beam ($\lambda = 1064$ nm). The circular polarization of the photon beam can be reversed using a rotatable quarter-wave plate. The optical setup is shown in Fig. 2.

To reach and maintain the maximum amplification of the photon density a feedback loop insures the locking of the laser frequency to the frequency of the cavity.

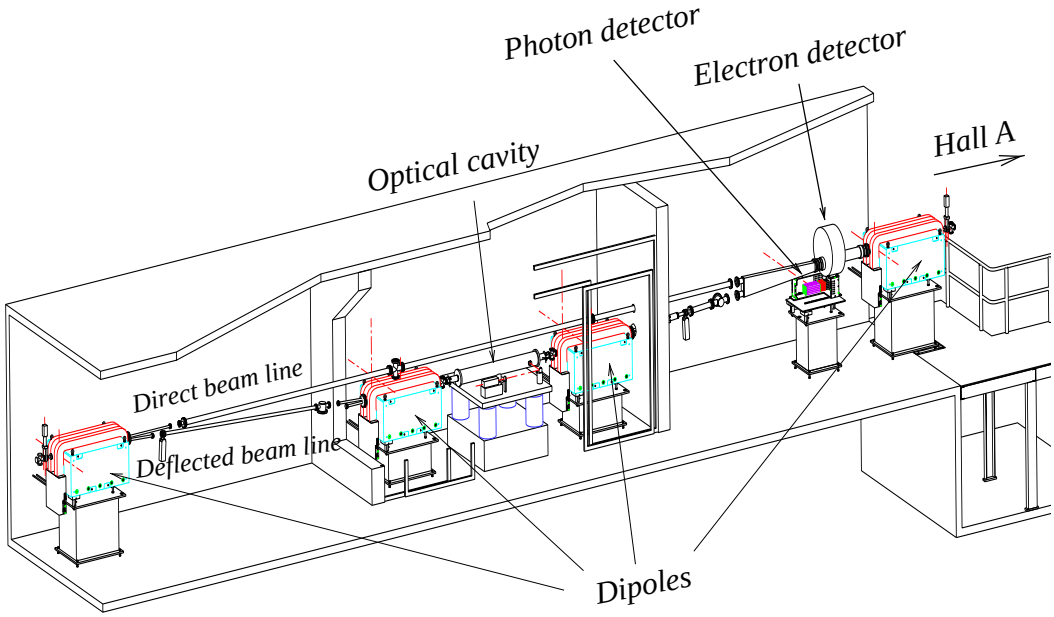

Figure 1: *Layout of the Compton polarimeter.*

This locking procedure is fully automatic and only requires a few seconds.

In order to maximize the Compton luminosity, the crossing angle between the two beams has to be a minimum. The design crossing angle of 23 mrad sets the mirrors about 5 mm away from the electron beam.

The overall opto-electronic system is controlled and commanded from the counting room.

An amplification factor of 7300 has been measured, corresponding to a photon beam power of 1700 W inside the cavity. The circular polarization was measured to be 99.3% $\pm$ 0.7 % for both right and left photon helicity states. Both the optical power and polarization remain stable for more than 10 hours.

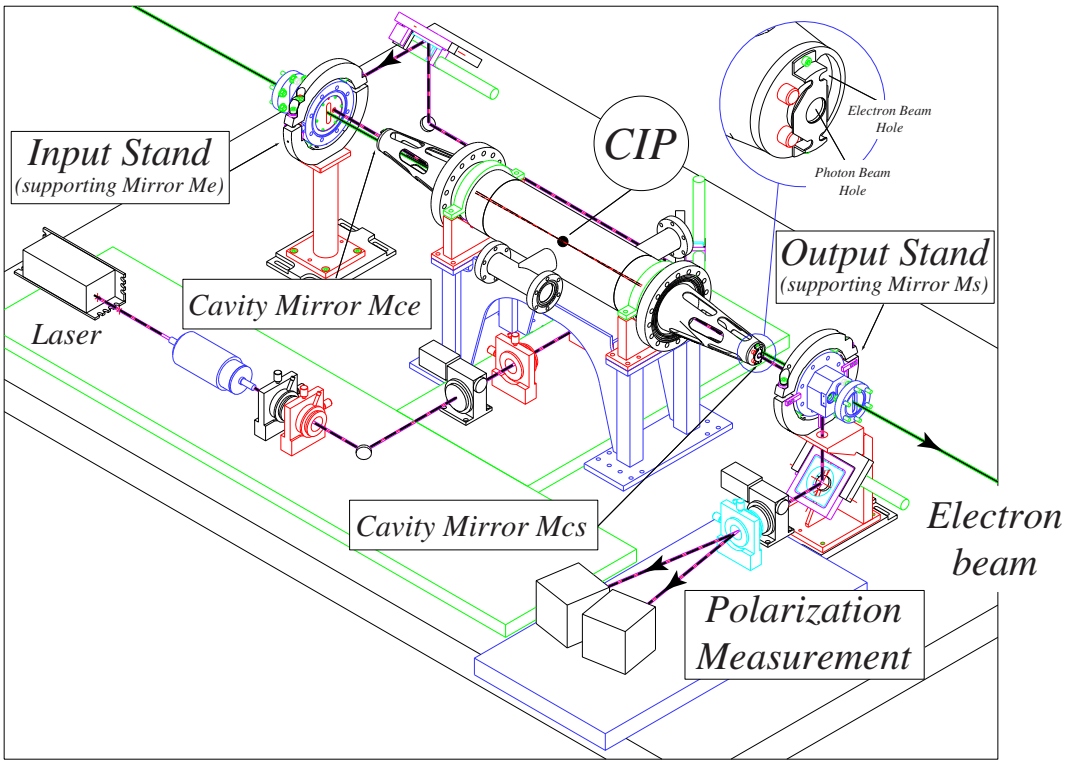

Figure 2: *3D view of the optics table with the monolithic cavity.*

1.4.4 First Evidence of Compton Events

With such a high photon density, Compton events could then be detected. In order to achieve this, the vertical position of the electron beam was scanned by varying the field in the dipoles until both beams crossed in the center of the cavity. Figure 3 displays the trigger rate recorded in the photon detector as a function of the vertical position of the electron beam. Evidence of Compton interactions was clearly observed in late February.

1.4.5 Preliminary Results for HAPPEX 99

The Compton polarimeter has been running concurrently with the HAPPEX experiment during April, May, and July, 1999. The beam energy was 3.3 GeV and the intensity about 40 μA.

Once the position of the electron beam had been tuned to maximize the Compton interaction rate, data were recorded for both photon beam polarizations. The background contribution was also measured without the photon beam. An asymmetry on the order of 1% was measured with a relative statistical accuracy of

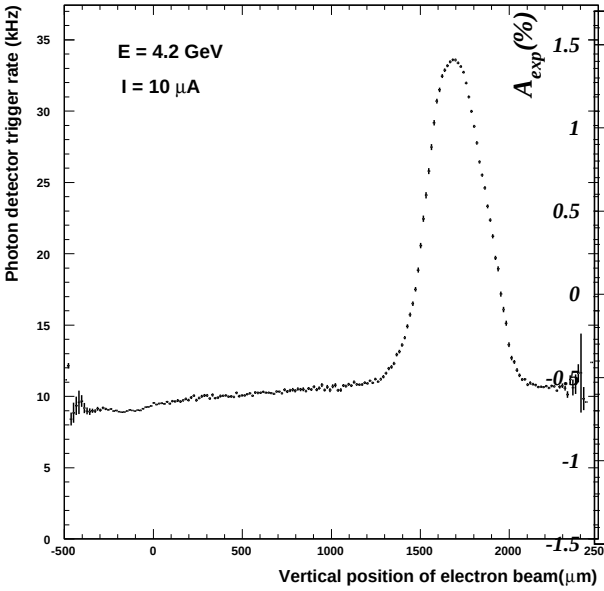

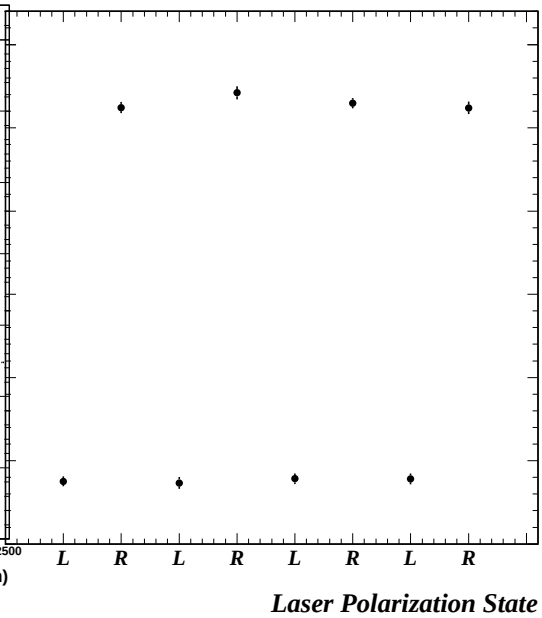

Figure 3: *Counting rate as a function of the vertical position of the electron beam inside the cavity.*

Figure 4: *Experimental asymmetry for right (R) and left (L) photon polarization.*

about 1% within an hour. Figure 4 shows the counting rate asymmetry measured in the photon detector for right and left photon polarizations. As expected, flipping the photon polarization reverses the sign of the experimental asymmetry.

The photon energy is also measured and one can reconstruct the energy spectrum of Compton backscattered photons (Fig. 5, black) and of the background events (grey). The background/signal ratio is about 0.1.

Preliminary results for data taken in May and July, 1999 are shown in Figs. 6 and 7. Only statistical error bars are shown. Data taken in April are not yet analyzed.

The analysis of the systematic uncertainties, such as background effects, photon detector resolution and calibration, and helicity correlated beam parameters, is underway. We aim to reach a 3% level for data taken during HAPPEX.

1.4.6 Skill Transferred to JLab Crew

Soon the operation and maintenance of the polarimeter will be the responsibility of JLab. Accelerator operators are already in charge of the Compton beam line. A staff physicist and technician will become responsible for the instrument. Specifically, technicians have already been familiarized with the optics and the vacuum system.

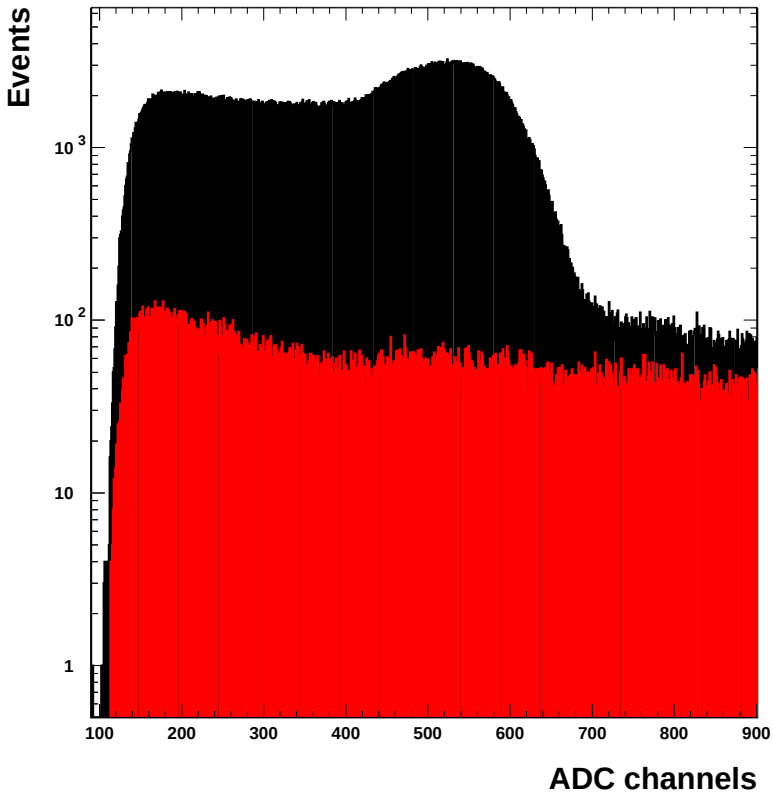

Figure 5: *ADC spectrum for signal (black) and background (grey).*

1.5 The Polarized ^{3}He Target (Contributed by J.P Chen)

The polarized ^{3}He target [1] is based on the spin-exchange principle: rubidium atoms in a vapor state in the pumping cell are polarized with optical pumping using three or four 30 W diode lasers for each polarization direction (longitudinal, transverse or any direction of choice). The polarization direction is defined with a magnetic field (about 25 Gauss) produced by two sets of main Helmholtz coils. The rubidium spin polarization is transferred to the ^{3}He nuclei by collision and then the polarized ^{3}He are transferred to the target cell where it is used for electron scattering experiments. The double-cell (pumping and target cells) target is made of aluminosilicate glass (either Corning 1720 or GE 180). The typical target length is 40 cm and ^{3}He pressure is about 10 atm at room temperature. The target polarization is measured and monitored using two different methods: NMR (nuclear magnetic resonance) with AFP (adiabatic fast passage), and EPR (electron paramagnetic resonance). Target data acquisition, monitoring, and control use both LabView and the EPICS systems.

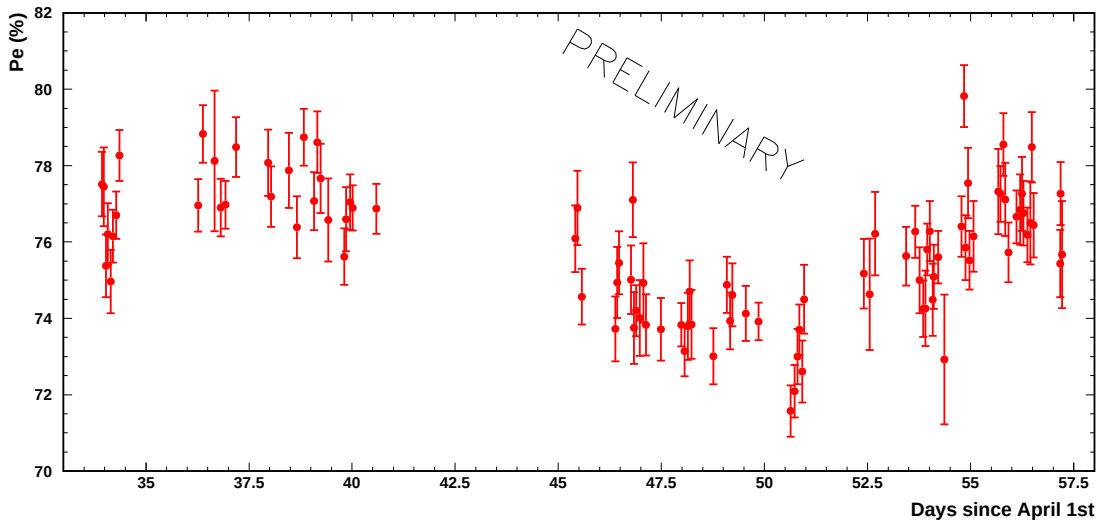

Figure 6: *Absolute value of the electron beam polarization as a function of time for HAPPEX data taken in May 1999. Errors are statistical only.*

The target was built last year, in a short time, by a collaboration from Caltech, Clermont-Ferrand, JLab, Kent State, Kentucky, MIT, Princeton, Temple, and William and Mary. It was successfully commissioned and used for the first two polarized ^{3}He target experiments (E94-010 and E95-001). During the first half of E94-010, there were a number of target glass cell ruptures, but since then the target worked very well allowing the two experiments to be successfully completed. The target polarization reached over 40% without beam and was between 30% and 40% with beam up to 15 μA. This was the first time this type of polarized ^{3}He target was run in such a high intensity electron beam.

The target was moved back into the target lab in EEL building after the completion of the two experiments. A number of tests (Q response study, temperature dependence study, field stability study, polarization loss study, etc.) have been performed to systematically study the target polarimetry methods. Further tests are planned in the next few months to fully understand the target performance and the systematics of the polarimetry methods. Improvements for the next round of experiments are under study. Some re-design will be needed and probably should get started, with some lead time, before the next round of polarized ^{3}He experiments.

The analysis of the polarimeter data from the first two polarized ^{3}He expriments is progressing well. The water calibrations required for NMR have been

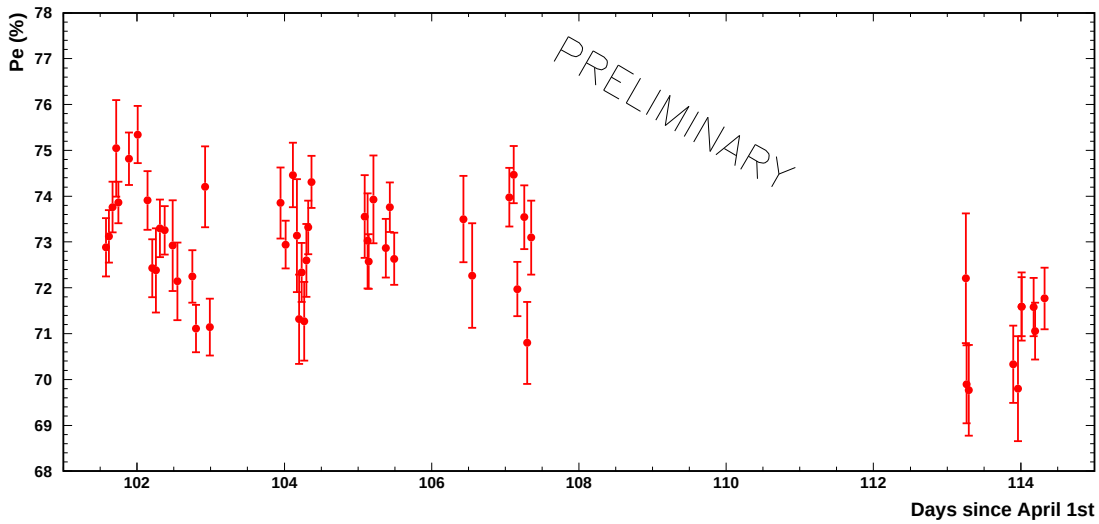

Figure 7: *Absolute value of the electron beam polarization as a function of time for HAPPEX data taken in July 1999. Errors are statistical only.*

analyzed thoroughly. All systematics have been studied. Final results are summarized in several technical notes[2]. The EPR analysis is still underway, but preliminary results are available. Final results with an analysis of the systematics are expected by the end of 1999. The preliminary results of the polarization during the experiment E94-010 are ready. Final results of the polarization during both E94-010 and E95-001 should be available soon after completion of the EPR analysis.

The heart of the polarized ^{3}He system is the target cell. Due to the complexity of the cell production and the difficulty involved in dealing with the aluminosilicate glass (such as Corning 1720), few places are able to produce target cells. For this collaboration, the Princeton group has been the only group which can produce the target cell. With the busy schedule of the Princeton group (especially their glass blower) and limited resources, it is highly desirable to have either JLab in-house capability or a near-by group to also be able to produce target cells. A joint effort between the William and Mary group and JLab is underway to set up a cell production facility at William and Mary. We expect to be ready to produce cells within about one year. Once the cell manufacturing capability is established, R&D effort to improve the target polarization will continue.

1.6 The Cryotarget (Contributed by M. Kuss)

The cryo target consists of 3 loops. Loop 3 can be filled with liquid hydrogen (LH_2), loop 2 with liquid deuterium (LD_2), and loop 1 with helium gas. The working conditions for all three loops are summarized in Table 10. Loops 2 and 3

Target	T/K	p/psi	$\rho/(g/cm^3)$
LH_2	19	26	0.0712
LD_2	22	22	0.162
^3He	5	220	0.93
^4He	5	220	0.92

Table 10: *Nominal working temperatures and pressures. The resulting densities are also listed.*

are equipped each with a cell block of a pair of "beer-can" type target cells which can be put into the beam alternatively. The short cell has a length of 4 cm, the long one of 15 cm, both have a diameter of 6.35 cm. Loop 1 has a single "tuna-can" type cell with a diameter of 10 cm.

A set of manual valves allows for the exchange of target materials between loops 1 and 3, e.g. loop 1 can also be filled with LH_2. For safety, during every run period any loop not in use is filled with ^4He at low pressure (15-50 psi), to prevent crushing of the target cells in case of vacuum failure or accidental venting.

It must be noted that it is impossible to operate the high-pressure helium and the liquid targets at the same time. The helium requires "5K" cryogen to achieve a high density, while the LH_2 and LD_2 targets use "15K" cryogen. Before helium target operation, hydrogen and deuterium have to be removed from the loops, to prevent freezing.

The 5K and the 15K cryogens are delivered through the same pipes, alternatingly. Separate coolant pipes would require a major redesign of the target which supports only three cold ports. Thus, change of cryogen will be done by plumbing at the distribution box in the End Station Refrigerator (ESR). This procedure may take a shift, plus one more shift for the preceeding warm-up and following cool-down.

The cryo target system was in-beam until August 1998 when it was replaced by the polarized ^3He target. It was successfully operated during E91-026 (deuteron), E93-050 (VCS), E91-010 (HAPPEX) and E93-027 (G_{Ep}/G_{Mp}), for a total of about 7 months in-beam.

During the cryo-target down time several modifications were done.

- The cell block in loop 1, which was identical to the ones in the other two loops, was replaced by the tuna-can type, as described above. This new cell block contains four additional Cernox (LakeShore) temperature sensors to improve the temperature monitoring of the helium gas.

- Bellows in the loop were replaced by new ones tested for high pressures.
- The three main temperature sensors of every loop, also Cernox, were replaced.
- New fans and tachometers were installed. The old tachometers didn't work at all.
- The coils for the low and high power heaters were replaced.
- The Oxford ITC502 temperature controller (reads the three Cernox and controls the low power heater) of loop 2 was replaced. Its controls were the suspected cause of the observed erratic behaviour of the low power heater, which disappeared after the modifications.
- During re-installation in March, the Input/Output Controller (IOC) dedicated to control the cryo-target stalled repeatedly. It was replaced by an identical board.
- The JT-valve control box was refurbished.

The tests performed in March showed that the fan of loop 2, the hydrogen loop at that time, performed badly. A replacement also did not work, and due to the pressing deadline it was decided to interchange the plumbing of loops 2 and 3 to have the LH_2 in loop 3, which was the only one used for the HAPPEX experiment.

In the June shutdown all three loop fans were checked. It turned out that fan 1 was also not working, and fan 3 started wearing out. Thus, again all three fans were replaced. Tests confirmed that all three performed well. As of this writing, during the run of E89-019, loops 2 and 3 are both in use, and are showing no signs of aging after almost two months in operation. Also during the shutdown a lead target, equipped with a platinum resistor, was installed on the solid target ladder to test a possible target design for future experiments.

In September 1998, the raster mode was changed from the rectangular to the circular pattern. HAPPEX found significantly more target boiling using the circular mode. Consequently, during the June shutdown the rectangular raster was reinstalled.

The preparations for the installation and the commissioning of the helium target scheduled for November and December are underway. The design of the gas handling system was finished in May, in August the gas panel assembly started and is almost completed. Only a few modifications on electronics and software controls are necessary. The additional temperature sensors require two additional ITC502 temperature controller, the valve control for the helium gas panel an additional SC200 board. Because more serial lines are needed an additional Octal card was installed. The work on the software controls is in progress.

1.7 Spectrometer Detector Package Development (Contributed by B. Wojtsekhowski)

1.7.1 Trigger Scintillators

The fast aging of the 8575 PMT observed during last year was a result of a large (up to 0.5%) concentration of helium in the hall. This was a particularly bad problem during the $^3He(e,e')$ experiment which used a helium jet to cool the target cell. In July 1999 the housings of all S1 and later all S2 PMTs were modified to prevent helium diffusion into the PMT by flushing the housing with nitrogen. The successful operation during the last three months indicates that the modification solved the problem.

The replacement of the model 8575 PMTs by the faster model R2083 achieved time resolutions of $\sigma_t = 0.13$ ns per counter. Figure 8 shows improvement of the β resolution on paddle number 5 ($X \sim 0.3\ m$) where fast PMTs were installed. The sigma of β is about 4.5% for the upgraded region in comparison 7.5% for the rest of HRS acceptance. However, the resolution is still not good enough for a stable separation of the beam bunches. JLab/UNH are developing a proposal for a new S1 plane with eight paddles of 1 cm thick plastic scintillators equipped with fast PMTs.

An additional counter S0 was built to allow 2 out of 3 trigger logic in the case

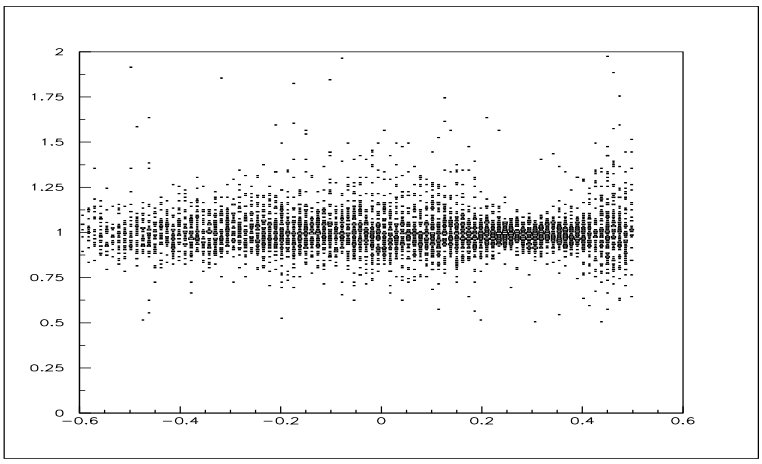

Figure 8: *Beta vs X position (in meters) on HA.*

of hadron detection. This counter is a single 170 cm long paddle 1 cm thick with 3 inch XP4312B on each end. Timing tests with cosmic rays for this counter gave a time resolution of $\sigma_t \sim 0.20$ ns.

The JLab electronics group has developed a CFD mounted on the HV divider of the R2083 PMT. We plan to test this CFD with a special thick scintillator

counter in the next couple of months and, pending the result, order a large number of CFDs for all new trigger counters.

1.7.2 Mirror Aerogel Detector (Contributed by J. Hovdebo)

The efficiency of the silica aerogel Cherenkov detector installed in the electron arm needed to be measured after it was put into operation. The efficiency is an exponential function of the number of photoelectrons collected by the photomultipliers. Therefore, the average number of photoelectrons produced by an event in the Cherenkov detector must be determined.

The photomultipliers do not have a linear response to the number of photoelectrons collected. Therefore, if the sum of all ADC's were taken, the most probable response would not correspond to a unique number of photoelectrons. By applying a correction on the ADC values, to force a linear response with photoelectron peaks occurring every 2000 channels, the average response is then linearly related to the average number of photoelectrons collected.

After the ADC's have been linearized, the average number of photoelectrons may be determined and the efficiency of the detector calculated.

Calibration of ADCs

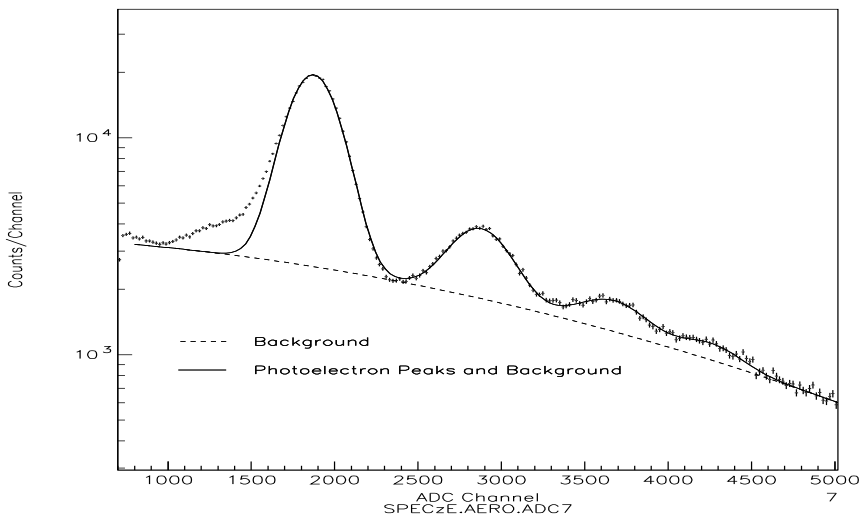

Figure 9: *ADC spectrum for a single photomultiplier fit with a Gaussian background and 4 Gaussians to represent photoelectron peaks.*

Data from Experiment 94-010, runs 1277, 1751, 1752, 2136, and 2642, for the reaction $^3\vec{He}(e,e')$ at incident electron momenta around 1.7 GeV/c were used to

perform the linearization of the ADC's. An ADC spectrum was generated, with a cut on the TDC suppressing the pedestal, for each of the ADC's in the detector. First, the background was fit using a first or second order exponential. The one, two, three, and if possible four, photoelectron peaks were then manually fit with Gaussians. The central values of the Gaussians were then taken as the positions of the photoelectron peaks. The result of such a fit is shown in Fig. 9. The desired 2000 channel gain/photoelectron was fit as a function of the measured photoelectron peak to second order. A minimum in the fit occurred, on average, around 1000 channels with the function increasing again for smaller responses. This effect causes the position of the first photoelectron peak to be obscured when the correction is applied. A dummy datum point at an abscissa value of 0 is introduced to move the minima of the correction closer to 0, without causing a large effect on the corrected peak positions. A sample fit is shown in Fig. 10. The

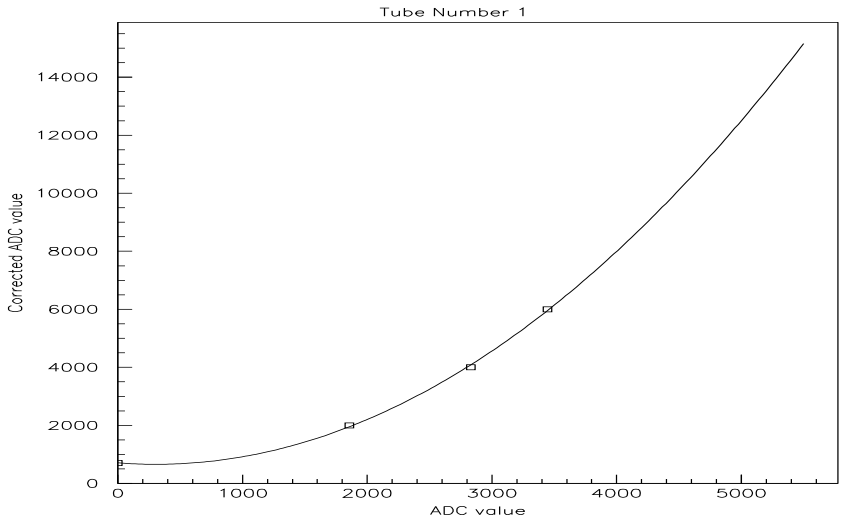

Figure 10: *Sample quadratic correction to linearize ADC response.*

ESPACE code was then modified to take into account the quadratic correction term and the coefficients of the fit were placed in the database file. ESPACE was then ran again to determine the effectiveness of the correction. Minor changes were made to improve the fit for the third photoelectron peak in the hope that this would better linearize the fourth and subsequent peaks where the non-linearity increases.

Calculation of Efficiency

With the corrected ADC values now giving a linear response, the ADC sum can be used to estimate the average number of photoelectrons collected. To speed

up calculations, the data are rebinned by a factor of 20 and the bins divided by 2000 to get the number of photoelectrons. A Poisson distribution was then fit to the data to determine the average number of photoelectrons.

To perform the fit, an integer number of photoelectrons is estimated for the most probable number of photoelectrons collected. A Poisson distribution of the form

$$y = \frac{\mu^x e^{-\mu}}{\Gamma(x+1)},$$

is fit, where y is the number of counts/channel, x is the ADC value, and μ is the mean value of the distribution. The data are then renormalized to place the peak at the estimated peak by the transformation

$$x_{data} = x_{data}\left(\frac{P}{x_{DataPeak}}\right).$$

The process of performing the fit and re-normalizing the data is iterated until a unique distribution is found. By choosing different initial values of photoelectrons, the best fit can be chosen and the corresponding most probable number of photoelectrons determined. In this manner, the most probable number of detected photoelectrons was found to be 6, corresponding to a mean number of collected photoelectrons of 6.3. The results of this procedure can be seen in Fig. 11 assuming most probable numbers of photoelectrons collected between 5 and 7. The true average of the data is found by multiplying, bin by bin, the ADC response by the number of counts/channel and summing and then dividing by the total sum of all counts. In this way, the average was determined to be 7.6. The difference in these two values being due to the long tail in the distribution of the data at large ADC values.

The efficiency of the detector may then be calculated through the formula

$$\eta = 1 - e^{-N_{pe}}.$$

Using the mean from the Poisson distribution fit the efficiency of the Cherenkov detector is calculated to be 99.82%, whereas the true average of the data, 7.6 photoelectrons, gives an efficiency of 99.95%

Conclusion

The average number of photoelectrons with $\beta = 1$ particles (electrons) has been extracted and determined to be 7.6. The photomultipliers exhibited a non-linear response which had to be corrected before this value could be extracted. A correction, to second order, was performed on the photomultipliers to force a linear response. The sum of all the ADC's was then fit with a Poisson distribution to give the mean number of photoelectrons collected. The efficiency was then found to be 99.95%.

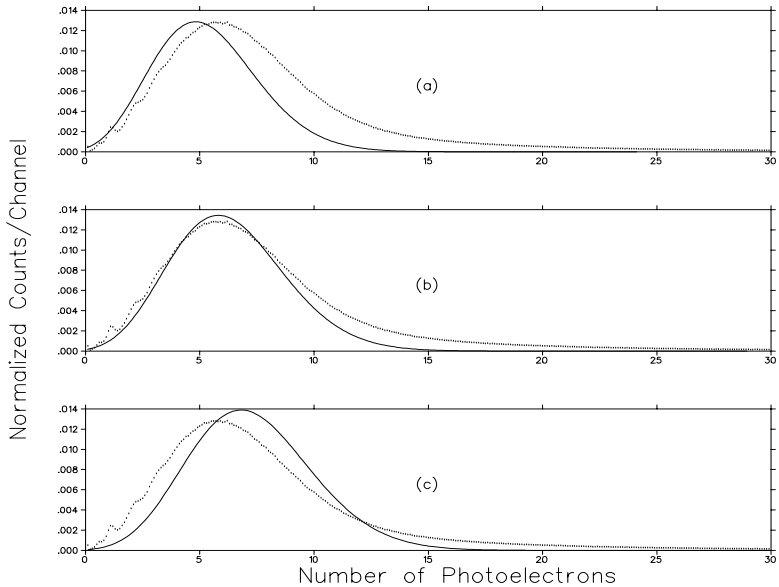

Figure 11: *ADC sum spectrum fit with Poisson distributions assuming different numbers of most probable number of photoelectrons: (a) Peak=5, $\mu = 5.3$, (b) Peak=6, $\mu = 6.3$, (c) Peak=7, $\mu = 7.3$*

1.7.3 Diffusion Aerogel Cherenkov Counter

The magnetic field in the detector hut at the location of the aerogel detector was found to be below 0.5 Gauss. Direct measurement of the PMT signal reduction there shows a small but stable 5% effect, see A. Leone and B. Wojtsekhowski, internal report 1998.

Weather conditions in Newport News require special attention to humidity control. A six PMT prototype was used to check the effect of aerogel baking on the light output. A large factor of about four was observed in the amount of light output from aerogel, see R. Iommi et al., internal report, 1999.

Direct measurement of the baking and humidity effects on the aerogel weight and light transmission (at 420 nm) show the necessity of keeping the air in the baking oven very dry during final stage of baking and of assembling the detector as fast as possible at as low as possible humidity, see A. White, JLab Technical Note 99-030. A plastic tent with DriTex dehumidifier was built to keep the humidity at a level 3-5% during assembly process, see Fig. 12.

A design of the 24 PMT aerogel detector was made based of the following considerations:
- complete hermetic sealing of the aerogel box and CO2 flushing;
- positive HV on the PMT for best geometry of the PMT face;
- no individual magnetic shields for best geometry of PMT face;

Figure 12: *Aerogel installation inside the dry tent.*

- double layer millipore paper coating of the interior of the detector;
- progressive HV divider for linearity of the PMT output.

A detailed study was done by using cosmic rays filtered through a cube of lead 2 feet on a side.

The detector performance was tested with beam in August with electrons and elastically recoiling protons. This test gave a direct measurement of the efficiency and rejection factors, which are the most important properties.

1.7.4 Diffusion Aerogel Cerenkov Counter Commissioning (Contributed by P. Markowitz)

Introduction

The kaon experiments (E94-107 and E98-108) require stringent particle identification to identify the true (e,e'K) coincidence reactions amidst high backgrounds of not only true $(e, e'\pi^+)$ and $(e, e'p)$ reactions but more frequently the accidental $(e, \pi^- \otimes \pi^+, K, p)$ coincidences. While true coincidence rates are less than 1 Hz, accidental rates of 1000 Hz or more will be prevalent for some kinematics.

A threshold diffusion aerogel detector (DAD) was built to provide separation of π^+ from kaons and protons, based upon their velocities. The detector has an active area of 160×22 cm^2 and was filled with aerogel with a nominal index of refraction of 1.025 (giving a nominal threshold of $\beta = 0.975$. The thickness of

the aerogel was either 3 cm for $-1.2 \leq x \leq 0.2$m or 9 cm for $0.2 \leq x \leq 1.2$m where x is the position in the focal plane along the dispersive direction and $x = 0$ corresponds to the central trajectory through the spectrometer.

Two rows of 12 photomultlier tubes (Burle 8854 five-inch tubes) lined both sides of the diffusion volume. The high voltage for the tubes was set (using cosmics rays for generating signals) to give approximately 70 mV signals into a 50 Ω terminal resistor for the single photoelectron peak. This corresponded to having the single photoelectron peak in channel 200 of the ADC.

Beam Tests

Electron beams of 3.3 and 5.5 GeV were used to commission the detector in August of 1999. The tests were meant to answer several questions:

- How many photoelectrons would result for β=1 particles (i.e., above threshold π^+ events in the kaon experiments)? For this test, the HRSh spectrometer was set to negative polarity and quasielastic electrons from ^{12}C were used to illuminate the detector broadly. Since every electron should give a signal in the DAD, the data determined the efficiency of the aerogel for detecting above threshold particles when a minimum number of N photoelectrons is imposed upon the data.

- How many photoelectrons would result for (subthreshold) β=0.9 particles (i.e., the kaons and protons in the experiments)? The kaons and protons should never fire the counter; however by creating knock-on electrons a fraction of the incident sub-threshold particles do give a signal in the DAD. This data determined the efficiency of the aerogel for detecting sub-threshold particles when a minimum number of N photoelectrons is imposed upon the data.

- What is the dependence of these efficiencies on the thickness of the aerogel? The aerogel has a very short scattering length and the light detected is not linearly proportional to the aerogel thickness, but the absorption depends on the number of bounces and amount of aerogel traversed.

Results

The results are displayed graphically in Figures 13a and 13b. Statistical error bars are hidden by the larger size of the plotting symbol. The systematic uncertainties are estimated to be on the order of 1-2% relative and are not shown. Plotted is the fraction of the events which result in a number of photoelectrons equal to or greater than a given value, as a function of the number of photoelectrons. This number imust also be corrected for the true location of the single-photon peak. For example, if the analysis requires in the 9cm region of aerogel that a minimum number of 3.5 photoelectrons is observed, $\sim$ 95% of the above threshold particles will fire the detector, however $\sim$ 5% of the below threshold particles will also be vetoed.

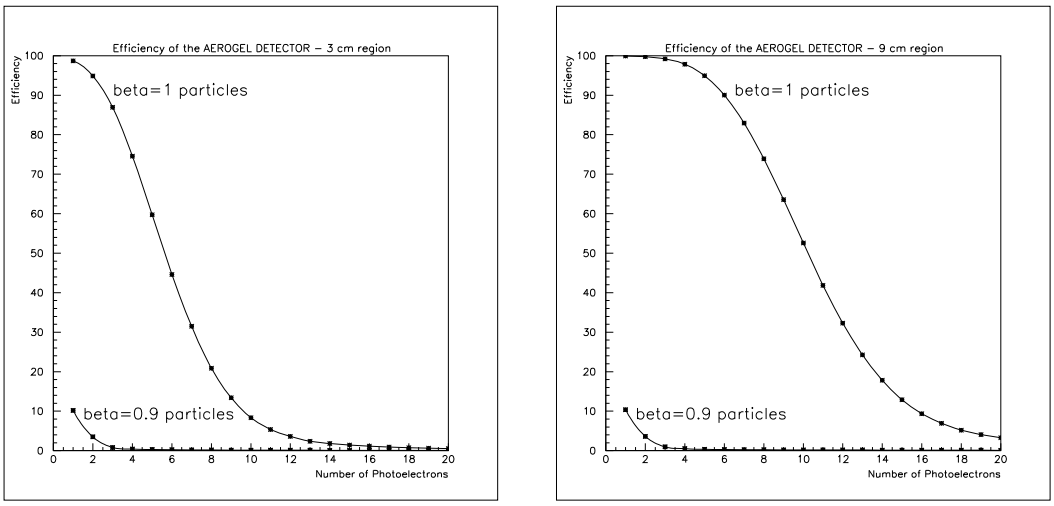

Figure 13: *The efficiency for β=1 and β=0.9 particles in the a) 3cm aerogel and b) 9 cm aerogel.*

Another interesting feature is seen by comparing the 3 cm data and the 9 cm data. The radiator thickness has increased by a factor of three, which would naively lead to an expectation of an increase by a factor of three in the average number of photoelectrons. This is not observed; instead, due to the combination of increased scatterings (due to the additional aerogel thickness with its attendant short scattering length) and subsequent absorbtion, the number increases by less than a factor of two. However the number of photoelectrons created by subthreshold particles is essentially unchanged, meaning that a thickness of 9 cm is preferred for this index of refraction of aerogel.

By placing a cut at 3 photoelectrons, the 9 cm data rejects 99% of the $\beta = 1$ particles, while only accepting 1% of the subthreshold particles, i.e., 99% of the $\beta = 1$ give more than 3 photoelectrons, while only 1% of the $\beta = 0.9$ subthreshold particles give more than 3 photoelectrons. Similarly, in the 3 cm data a cut placed at approximately 1.75 photoelectrons will reject 96% of the the $\beta = 1$ particles, while accepting only 4% of the subthreshold particles, i.e., 96% of the $\beta = 1$ give more than 1.75 photoelectrons, while only 4% of the $\beta = 0.9$ subthreshold particles give more than 1.75 photoelectrons in the 3 cm region of aerogel. These are quite impressive performances.

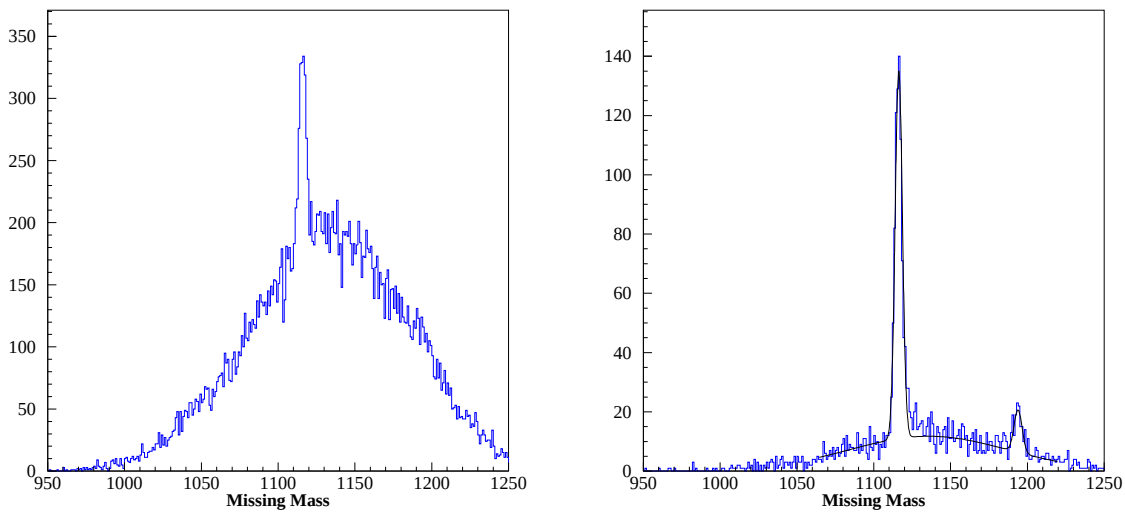

Figure 14: *The (e,e'K) missing mass spectrum a) without and b) with a cut on the pulse height in the aerogel detector.*

Figure 14 shows the missing mass spectrum (a) without and (b) with a cut on the pulse height in the aerogel detector. Without any cuts, the pions (mainly true $(e, e'\pi^+)$ coincidences) form a dominant background, although the Λ peak is still clearly seen. With the cut, the background is greatly reduced, and shows the Σ^0 peak as well. The remaining background is mainly accidental (e,e'p) coincidence reactions. A second aerogel with a higher index of refraction (designed to fire on both kaons and pions but not protons) will reject the remaining background.

Conclusions

A threshold diffusion aerogel detector has been commissioned. The results show that the efficiency using 9 cm of aerogel will give a good rejection (99%) of π^+ events in the upcoming experiments. Based upon these results, a second diffusion aerogel box using a radiator with a larger index of refraction will be constructed to reject protons. Additionally, two kinematics have been taken where the existing diffusion box was used to produce a $H(e, e'K^+)\Lambda^0$ spectrum. Those data are still under analysis and additional results will be presented soon.

1.7.5 Vertical Drift Chamber

The algorithm for data based calibration of the time-to-distance conversion was developed and tested (with K. Fissum). The resulting table allows a fast and nearly perfect conversion, as shown in Fig. 15. The main ideas are to use the global angle for corrections and symmetric events ($t_i = t_{i+1}$ *and* $t_{i-1} = t_{i+1}$) for fixing the x/t calibration parameters. A complete discussion of both this algorithm

and entire VDC project will be presented in a forthcoming technical note.

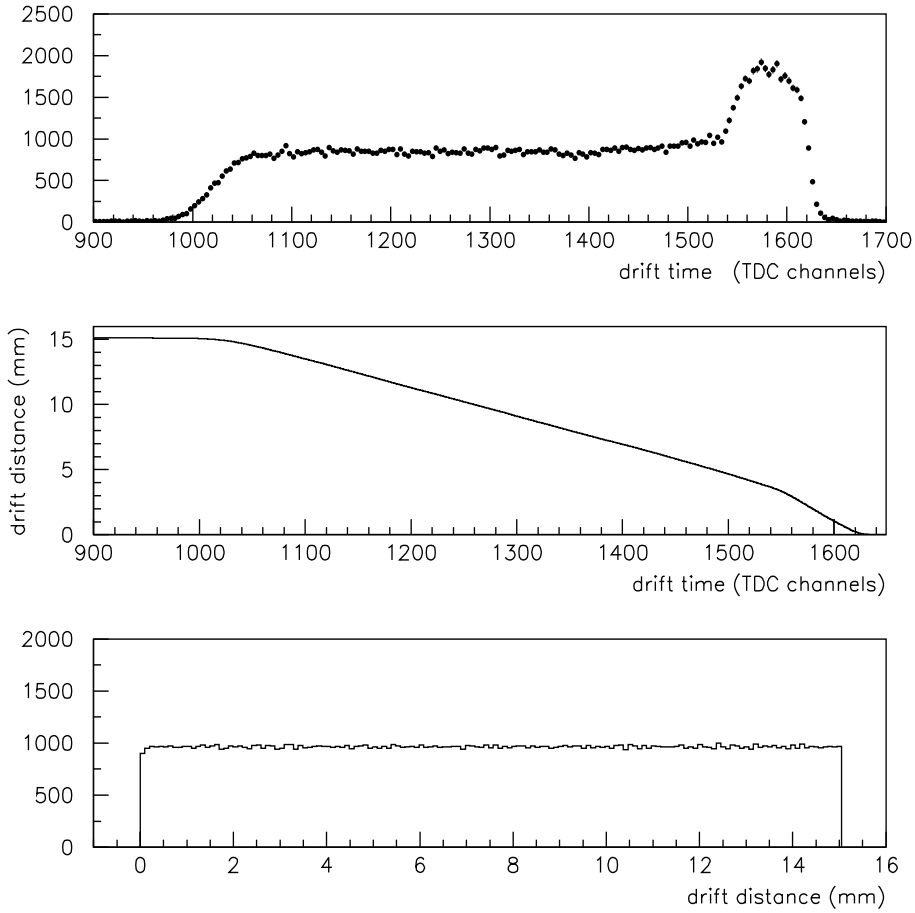

Figure 15: *VDC time-to-distance conversion.*

1.7.6 Gas Cherenkov Counter

A study of the gas cherenkov (GC) performance found the following. A uniform voltage distribution on the 8854 PMT led to nonlinearity in the GC output, even for relatively small anode signals because in each event the photons are focused on a small ($\sim$1 cm^2) area of the PMT photocathode. For a correct counting of the number of the photoelectrons the average amplitude of the single photoelectron signal should be used for normalization, not a peak value, as was done in many previous analyses, see e.g., the study by M. Shephard and A. Pope, JLab Technical Note 97-028. A MC simulation of the amplitude distribution using the experimental distribution of one photon response and Poisson distribution for photon counting as inputs, agreed well with the observed amplitude distribution, see

the code and results by J.McCann, JLab Technical Note 98-027. A P-terphenyl coating increases the number of detected photoelectrons by a factor of up to 1.3 for Burle 8854 PMT, see S.Duncan et al., JLab Technical Note 98-006.

1.7.7 Pion rejector

Figure 16: *Pion Rejector counter.*

For redundant pion/electron identification on the Hadron arm during $^3He(e,e')$ experiments a lead-glass based pion rejector was built, see Fig. 16. We used spare lead glass blocks 15x15x30 cm left from Electron arm shower detector. The amplitude distributions for the pions and electrons (bottom) are shown in Fig. 17. The acceptance coverage (right) and the acceptance holes (left) are shown in Fig. 18.

1.7.8 Large Scintillator Arrays

The proton yield in electroproduction was measured using 16 large plastic counters from ITEP. The results were about a factor 1.5 to 2 lower than a MC prediction by P. Degterenko.

For a study of nucleon correlations UVa built neutron bars which were assembled in the form of a 7x11 package. This package was used to evaluate luminosity limitations with a large open detector "Third Arm". Fig. 19 presents the current from individual PMT which is proportional to the light emission in the given counter. The front wall gets $\sim$ 50 times more background than the inner bars.

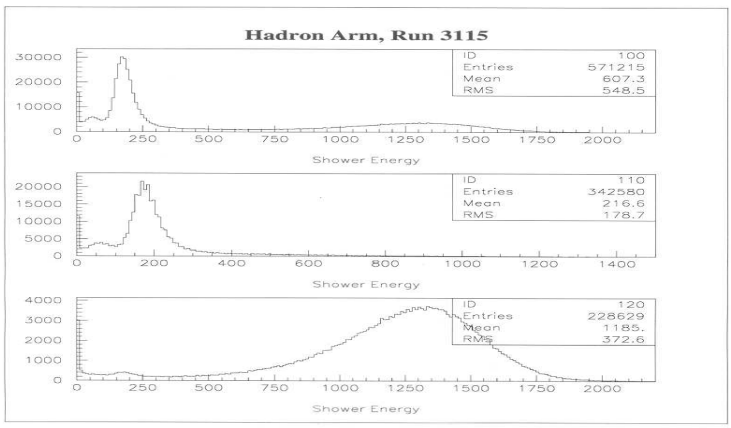

Figure 17: *Pion Rejector Amplitudes*

The outer side detectors have about double the current of inner detectors. For more information see http://erwin.phys.virginia.edu/research/groups/thirdarm.

1.7.9 Big Bite detector package

On August 16, 1999 a workshop was held where several experiments which might use the Big Bite detector were discussed. Pion threshold electroproduction can be done at low luminosity with the present detector system, but many other require a 10^{38} /cm^2/s luminosity and a new highly segmented detector. A proposal for a new detector is under development.

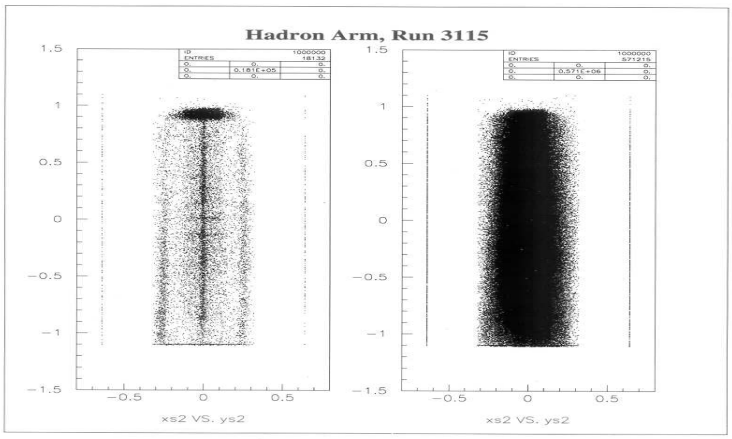

Figure 18: *Pion Rejector Acceptance.*

1.8 Data Acquisition and Trigger (Contributed by R.O. Michaels)

This section explains the progress and problems in DAQ and triggers, and outlines the plans for the near future. Everyone is reminded that up–to–date information on status, structure, and usage are at
www.jlab.org/Hall-A/equipment/daq/daq_trig.html.

In the past year, there were two main improvements in the DAQ: (1) We deployed the capability of making the two HRS read out independently, which approximately doubles the speed for single–arm experiments. (2) The networks involved in our two "high performance" systems (HRS and Compton DAQ) were upgraded with better isolation (subnetting and localized resources), new switches and gigabit routers. In some specific instances, problems on external systems had been observed to slow down the DAQ. The upgrades cut down on these interferences.

A problem noted about the trigger is that many of the commercial modules we use are no longer manufactured. We are currently seeking long–term solutions. One example is that our leading–edge discriminators, which are no longer made by LeCroy, will eventually be replaced by constant fraction discriminators which should improve the time resolution. Bogdan Wojtsekhowski is working on this. Another problem noted is that software to analyze the trigger efficiency, logic, and timing is not standardized in ESPACE. Each experiment creates their own version, and there is virtually no transfer of knowledge nor of software. New online software is being written which will help correct this situation.

In the near future, the following upgrades are planned: (1) In November 1999, a new "burst mode" ADC will be deployed for reading out the BPM and raster information. It will replace the ADC modules which had the infamous

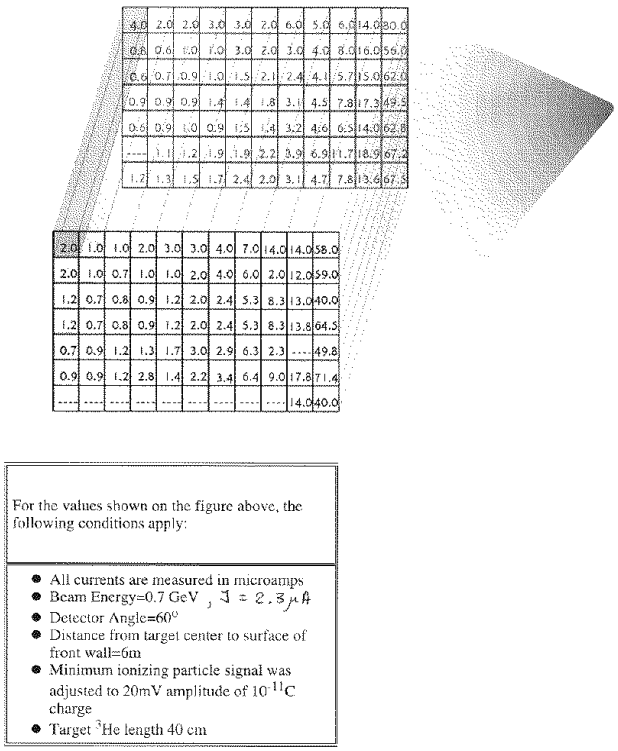

Figure 19: *Anode currents in 7x11 package.*

synchronization problems noted during VCS experiment. In each event typically 5 samples will be read out at 1 MHz, so that both the amplitude and phase can be determined unambiguously. (2) In the January shutdown, all the RS232 terminal servers will be replaced. (3) Also in January, we will upgrade CODA to use the ET event distribution system. This will improve the real–time distribution of events to online software.

Another major effort in the next year is the setup of a DAQ system for a "third arm" spectrometer, in this case the calorimeter and associated detectors for the Real Compton Scattering experiment. Physicists from the University of Illinois and JLab are collaborating to make this DAQ system and integrate it with the HRS DAQ.

1.9 Analysis Software (Contributed by J-O Hansen)

Users currently use the FORTRAN-based ESPACE[4] was originally developed at Mainz and later refined at MIT before being introduced in 1995/96 by E. Offerman. It is written in FORTRAN 77 with VAX-style extensions (e.g. structures). Its capabilities include:

- Reading raw event data, mapping them to logical structures, and analyzing them in terms of physics quantities (e.g. hits, photoelectrons, four-vectors, kinematics).
- Dynamic definition of conditional tests (cuts) and application of these to select event data.
- Dynamic definition of histograms and ntuples and output of these in HBOOK format.
- Fitting of analysis parameters to experimental data ("optimization").
- Displaying single events in terms of detector hits in a graphics window.
- Program control and analysis steering via KUIP.

Dynamic definition of tests and histograms is accomplished by the COOLHANDS package [3] which can be accessed from KUIP. The wire-chamber track-fitting code in ESPACE is quite advanced and is usually more accurate, although also considerably slower, than similar readily available algorithms. ESPACE is available on HP-UX, SunOS, Alpha/OSF, and Linux. It does not currently work under AIX.

ESPACE has been used to date by almost all experiments for production data analysis. The program is actively maintained; new versions are released every several months and include bug fixes and relatively minor improvements. It is common for experiments to customize the "official" ESPACE for their specific needs.

The experience with the package has generally been good. ESPACE's main advantages are that it is relatively well debugged after several years of use and has been adapted for the specific hall requirements. However, a number of complaints have been raised, including:

- Speed: ESPACE is relatively slow compared to similar programs, given the fact that the detectors are only moderately complex. Typical analysis rates on a fast Linux machine are 100-200 events/s.

[4] Event Scanning Program package for data analysis. While ESPACE generally performs well, it has a number of shortcomings concerning speed, flexibility, and maintainability. To address these issues, we are in the process of redesigning its analysis software using object-oriented programming concepts. The implementation of the new analyzer will rely on the ROOT system, developed at CERN, and the C++ programming language.

1.9.1 ESPACE

Our current physics analysis software ESPACE for Hall A Collaboration Experiments

- Flexibility: ESPACE's rigid structure makes it difficult to modify the program, e.g. to add new detectors.
- Maintainability: ESPACE is hard to maintain due to its monolithic program structure, the FORTRAN 77 language, and use of unversioned text-based database input files.
- Documentation: Detailed programming information and documentation of algorithms is sparse, adding to the difficulty to maintain the package.
- Portability: Extensive use of VAX-style, non-standard FORTRAN requires special, commercial compilers and limits portability (e.g. AIX).
- ESPACE relies heavily on CERNLIB, KUIP, and HBOOK, which, although currently still supported by CERN, are headed for obsolescence.
- Limited capabilities: No real-time (online) viewing. Optimizations do not work in some cases. COOLHANDS has only limited functionality for arrays and 2-dim histograms.

Among these, the first four are particularly important in view of upcoming detector upgrades. Unfortunately, improvements would require a significant effort and might result in large sections of the code being essentially rewritten.

1.9.2 The Object-Oriented Analyzer

In May 1999, after evaluating several options for the future of our analysis software, the code development team[5] decided to start the design of a new analyzer using object-oriented programming concepts implemented in C++. This new analyzer will rely, at least partly, on the ROOT system [4], an object-oriented framework that has been under development at CERN since 1995 and has been adopted by several major collaborations at FNAL, BNL, and elsewhere.

ROOT is frequently considered the "successor of PAW", but actually offers much more functionality than just interactive data analysis, viz. object-based I/O, complex data structures ("trees"), multi-dimensional histogramming, an interactive C++ interpreter (CINT), database, client/server and parallel processing facilities, and support for dynamic linking, to name a few. ROOT currently has about 500 active users worldwide. Extensive documentation is available on the Web [5]. Since many physics-specific capabilities (e.g. histogramming, data structure I/O) have already been implemented in ROOT, they do not need to be reinvented for our purposes; and, since ROOT is being used by several other major collaborations, a wide code base as well as support is readily available.

The design of the new, object-oriented analyzer is currently in progress and expected to converge towards the end of this year. A first working version could be available as early as mid-2000. The design goals are, obviously, to provide the

[5] W. Boeglin (FIU), J.-O. Hansen (JLab), J. Templon (Georgia), P. Ulmer (ODU)

functionality of the current ESPACE (however, not necessarily all included in a single monolithic program) and to improve on most of the identified shortcomings of ESPACE. Particular emphasis will be placed on flexibility to accommodate changing detector configurations.

Manpower currently consists of three staff members, each contributing between 30-70% of their time. Several other people have expressed interest in contributing at later stages of the project. Some collaboration with Hall C as well as the JLab DAQ group is also expected.

1.10 Optics Commissioning (Contributed by N. Liyanage)

Thanks to a lot of planning and hard work by many people we now have good optics databases that cover a large fraction of the momentum range of the HRS pair. During the last few months we have taken data required to calibrate the spectrometers at the remaining momenta. We are hoping to finish the analysis of this data by the end of the year. These would complete the set of databases that would cover the available momentum ranges of the HRS pair.

The optics data used for the recent optimizations were acquired during experiments E93-050 (VCS) and E94-010 (GDH). During these optimizations several improvements to the ESPACE optimizations procedures were made. These improvements would be extremely useful for the future optimization projects.

1.10.1 Databases at 0.85 GeV/c

The linear range of the high resolution spectrometers extends up to $\sim$ 3.0 GeV/c. Thus a database optimized at 0.8 GeV/c works well over this whole range. The optics data obtained during the GDH experiment with a ^{12}C target stack covering the full y_{tg} range of the spectrometers were used to optimize the databases for both HRSe and HRSh at 0.85 GeV/c. As expected the obtained databases work well from 0.4 GeV/c to 3.0 GeV/c for the whole y_{tg} range of $\pm$ 5 cm.

1.10.2 HRSe Databases above 3.0 GeV/c

The optics data taken during the VCS experiment provided the opportunity to optimize the HRSe optics database at 3.0 GeV/c and 3.5 GeV/c. These databases have similar resolutions and accuracies as the databases obtained at lower momenta. However the y_{tg} coverage is limited.

1.10.3 Summary of available databases

Spectrometer	Database	P range	Y_{tg} range
	0.85 GeV/c	up to 3.0 GeV/c	$\pm$ 5.0 cm
HRSe	3.0 GeV/c	2.8 GeV/c - 3.4 GeV/c	$\pm$ 3.0 cm
	3.5 GeV/c	3.3 GeV/c - 3.7 GeV/c	$\pm$ 2.0 cm
HRSh	0.85 GeV/c	0.4 GeV/c - GeV/c	$\pm$ 5.0 cm

Table 11: *Spectrometer Database Summary.*

We have taken optics calibration data for HRSe at 4 GeV/c and for HRSh at 2.75 GeV/c. This data is being analyzed now.

Listed below are the accuracies and resolutions achieved with the available databases:

For 0.85 GeV/c electrons scattered off a thin ^{12}C target

- Angle determination accuracy
  - Transverse 0.15 mrad
  - Dispersive 0.5 mrad
- Angular resolution (FWHM)
  - Transverse 1.5 mrad
  - Dispersive 6.8 mrad
- Momentum resolution (FWHM)

  For $y_{tg} = 0$ 3×10^{-4}

  Overall 4.5×10^{-4}
- Transverse position determination

  $\pm$ 0.5 mm
- Transverse position resolution

  4.0 mm

The above angular and position resolutions are close to what can be expected at 0.85 GeV/c for this target configuration. However, the momentum resolution is about a factor of two worse than expected. This can be attributed to the beam energy spread which has been measured to be about 2.5×10^{-4} (FWHM). Improvements in the beam energy width is expected to improve the momentum resolution to about 1×10^{-4} (FWHM) at the middle of the focal plane and to about 3×10^{-4} (FWHM) overall at 0.85 GeV/c.

1.10.4 Spectrometer constants calibration

The HRS spectrometer constants (Γ) were previously known only at about the 2×10^{-3} level. The precision beam energy measurements using EP and Arc have made it possible to measure the spectrometer constants much more accurately. Therefore whenever a beam energy measurement was performed we have gathered data necessary for the calculation of Γ.

We use two methods to calculate the Γ's:

- The direct method, where we measure elastic scattered electrons from ^{12}C to directly calculate Γ for that spectrometer.
- The indirect method where we measure the missing energy of $1p_{1/2}$ state in $^{12}C(e, e'p)$ coincidence data. We then use this information with the already measured spectrometer constant of one spectrometer to derive Γ for the other spectrometer.

Using these two methods we have calculated the spectrometer constants of the two spectrometers at the momenta summarized below. We are planning to take more data in the next few months which would allow us to calculate the spectrometer constants of both spectrometers over the full momentum ranges to 4×10^{-4} accuracy. Once both spectrometer constants have been measured to this level, a short ^{12}C$(e, e'p)$ run can be used to calculate the beam energy to a similar accuracy eliminating the need to perform energy measurements frequently.

The tables below summarize the spectrometer constant values we have calculated with the available data.

Momentum (GeV/c)	Γ_{HRSh}	
2.73	269.4 ± 0.15	^{12}C(e,e'p)
1.88	269.2 ± 0.2	^{12}C(e,e'p)
0.61	268.4 ± 0.9	H(e,e'p)

Table 12: Γ_{HRSh}

Momentum (GeV/c)	Γ_{HRSe}	
1.26	270.1 ± 0.1	^{12}C(e,e)
3.88	269.9 ± 0.2	^{12}C(e,e'p)

Table 13: Γ_{HRSe}

2 Summaries of Experimental Activities

2.1 E89-003

A Study of the ^{16}O$(e, e'p)$ Reaction in Quasielastic Kinematics

W. Bertozzi, R. Lourie, A. Saha and L. Weinstein, Spokespersons,
and
the Hall A Collaboration.

Experiment 89-003 was the first physics experiment in Hall A. The experiment took place in the summer of 1997 and the data analysis was completed by the end of 1998. A letter on the 1p state results has been submitted for publication and a letter on 1s state results is in preparation. [6,7]

In this experiment, we measured the ^{16}O$(e, e'p)$ reaction in the quasielastic region at $|\vec{q}| = 0.992$ GeV/c and $\omega = 439$ MeV. We extracted the longitudinal (R_L), transverse (R_T), and longitudinal-transverse interference (R_{LT}) response functions from cross sections measured at several beam energies and electron angles for $E_{miss} < 60$ MeV and $P_{miss} < 355$ MeV/c. This was the first response function separation on a complex nucleus at large E_{miss} and P_{miss}.

We scattered the continuous incident electron beam from a waterfall target [8] and detected the scattered electrons and knocked-out protons in the High Resolution Spectrometers.

We measured the ^{16}O$(e, e'p)$ cross sections at three beam energies keeping $|\vec{q}|$ and ω fixed in order to separate response functions and understand systematic uncertainties (see Table 14). For $\theta_{pq} = \pm 8°$, R_{LT} and A_{LT} extracted at $E_{beam} =$ 2.4 GeV agree with those extracted at $E_{beam} = 1.6$ GeV within one standard deviation. The overall systematic uncertainty in the extracted response functions is about 5%. This uncertainty is dominated by the uncertainty of the H(e, e') cross section to which the data were normalized [9].

The accuracy of a response function separation depends on precisely matching the values of $|\vec{q}|$ and ω between different kinematic settings. In order to match $|\vec{q}|$, we measured H$(e, e'p)$ (also using the waterfall target) with a pinhole collimator in front of the HRS$_e$. The momentum of the detected protons was thus equal to $\vec{q}$. We determined the location of the H$(e, e'p)$ momentum peak to $\frac{\delta p}{p} = 1.5 \times 10^{-4}$, allowing us to match $|\vec{q}|$ to 1.5×10^{-4} between the different kinematic settings. Throughout the experiment, H(e, e') data, measured simultaneously with the ^{16}O$(e, e'p)$ data, provided a continuous monitor of both luminosity and beam energy.

The radiatively corrected ^{16}O$(e, e'p)$ cross section as a function of missing energy for $E_{beam} = 2.4$ GeV at $P_{miss} \approx 60$ MeV/c is shown in Fig. 20. The two prominent peaks at $E_{miss} = 12.1$ and 18.4 MeV correspond to protons knocked-out from the $1p_{1/2}$ and $1p_{3/2}$ states. The missing energy resolution is 0.9 MeV

FWHM. The peak at 22 MeV is a cluster of $1p_{3/2}$ states. The broad peak centered at $E_{miss} \approx 42$ MeV is due to proton knockout from the $1s_{1/2}$ state.

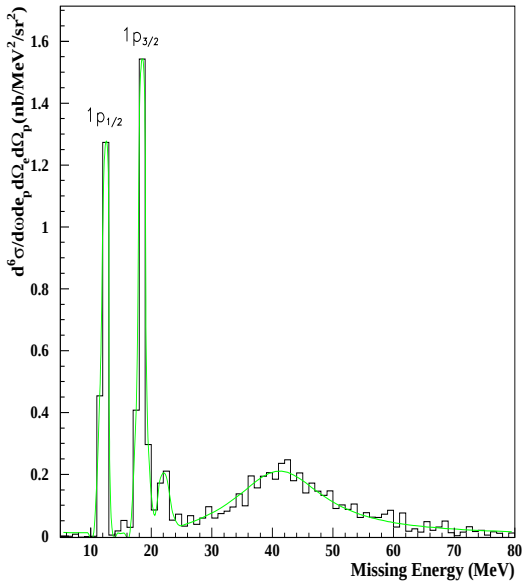

Figure 20: *Measured* $^{16}O(e,e'p)$ *missing energy spectrum for* $E_{beam} = 2.4$ *GeV at* $P_{miss} = 60$ *MeV/c.*

Figure 21 shows the measured momentum distribution at $E_{beam} = 2.4$ GeV. The calculations of Udias are in excellent agreement with the data, whereas the calculations of Kelly are in good agreement up to $P_{miss} = 280$ MeV/c.

We extracted the left-right asymmetry ($A_{LT} = \frac{\sigma(\phi=0^\circ)-\sigma(\phi=180^\circ)}{\sigma(\phi=0^\circ)+\sigma(\phi=180^\circ)}$) from the measured cross sections (see Fig. 22).

To determine how much of the observed continuum strength can be explained by $1s_{1/2}$-state knockout, we compared our results to single-particle knockout calculations by Kelly [12], and Ryckebusch [13–15].

Fig. 2.1 shows the cross sections measured over the entire range of P_{miss} probed by this experiment. The cross sections are compared to $1s_{1/2}$-state single-particle knockout calculations by Kelly folded with a Lorentzian shape with an energy-dependent width [16,17]. At $\langle P_{miss} \rangle = 50$ MeV, the Lorentzian shape exactly describes the measured cross section.

As P_{miss} increases, the single-particle knockout calculation accounts for only a fraction of the measured strength. Furthermore, for the two settings with P_{miss} above the Fermi-momentum of ^{16}O (≈ 220 MeV/c), the measured cross section profiles do not exhibit any resemblance to the expected single-particle Lorentzian shape. This clearly indicates that the cross section measured at high E_{miss} and high P_{miss} is mostly of non-single-particle origin.

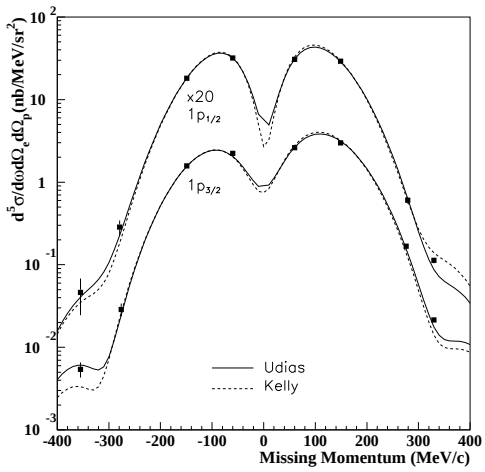

Figure 21: *Measured cross sections and DWIA calculations at* E_{beam} *= 2.4 GeV. The solid line is the Udias* et al. *calculation [10], and the dashed line is the Kelly calculation [11]. The* $1p_{1/2}$ *state cross section and calculations have been multiplied by a factor of 20.*

Figure 24 presents the separated response functions for the high E_{miss} region of the $\theta_{pq} = 0°$ kinematic setting. The difference between the transverse and longitudinal spectral functions ($S_T - S_L$), which is expected to be zero for a free nucleon, is nonzero for $E_{miss} > 40$ MeV. This is in qualitative agreement with the high-E_{miss} behavior of R_L and R_T observed at MIT-Bates by Ulmer *et al.* [18] and also at Jefferson Lab in Hall C [19].

E_{beam} (GeV)	θ_e (°)	θ_{pq} (°)
0.843	100.7	0, 8, 16
1.643	37.2	0, ±8
2.442	23.4	0, ±2.5, ±8, ±16, ±20

Table 14: *Experimental Kinematics*

In summary, we have measured, in a previously inaccessible region of momentum transfer, cross sections, the left-right asymmetry A_{LT}, and the response functions R_{L+TT}, R_{LT}, and R_T for $^{16}\text{O}(e,e'p)$ proton knockout for missing momentum less than 355 MeV/c. Data analysis has been completed and publications have been submitted.

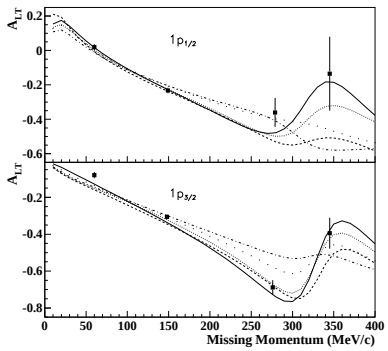

Figure 22: *The dashed line is the Kelly calculation [11]. The other curves are from Udias* et al. *[10]. The solid line is the fully relativistic calculation, the close dotted line is that with only the bound-state spinor distortion included, the wide dotted line is that with only the scattered-state spinor distortion included, and the dot-dashed line is that without spinor distortion included.*

2.2 E89-033

Limits on Changes in G_E^p/G_M^p in the Nuclear Medium from the $^{16}\mathrm{O}(\vec{e}, e'\vec{p})$ Reaction

Charles Glashausser
and
The Hall A Collaboration

The longitudinal (P_L) and transverse (P_T) components of the polarization of the recoil proton in the $^{16}\mathrm{O}(\vec{e}, e'\vec{p})$ reaction are sensitive to the electromagnetic form factors G_E^p and G_M^p of the proton in the nuclear medium. The ratio of these polarization components can be measured with little systematic error since the polarization of the beam and the analyzing power of the proton polarimeter cancel in the ratio. This ratio is then a robust measure of possible changes in the form factor ratio in the nuclear medium, since many corrections to the Impulse Approximation are also minimized. E89-033 is the first application of this technique to a complex nucleus.

The experiment was run in the summer of 1997, as part of the commissioning of Hall A. This experiment also functioned as a commissioning activity for the polarized beam at JLab, and for the focal plane polarimeter. The data have now been analyzed, and compared with several theoretical calculations. The results are described in the Ph.D. theses of two students, Sergey Malov and Krishni Wijesooriya, who have successfully defended in September at Rutgers and in May at

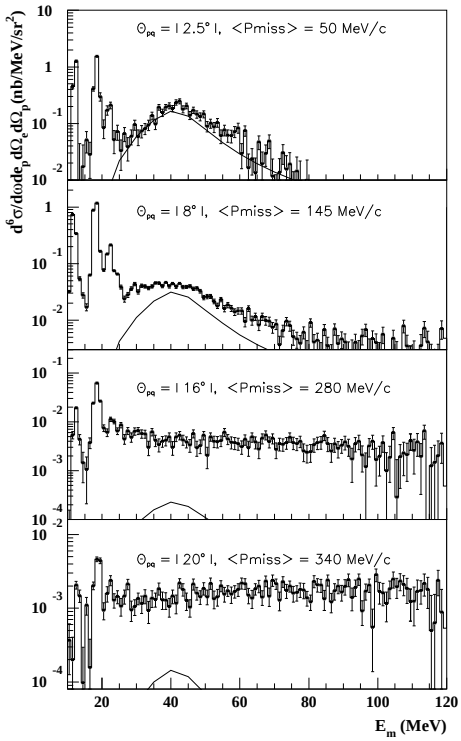

Figure 23: *Cross sections measured at different missing momenta as a function of missing energy. The curves show the $1s_{1/2}$-state single-particle strength calculated by Kelly folded with the Lorentzian parameterization of Mahaux.*

William & Mary, respectively. Preliminary results have been presented in invited talks at conferences up to May, 1999. A paper is currently under preparation.

The results of the 1997 run yield a result for the ratio of G_E^p and G_M^p in the nuclear medium which is consistent with its free value with an uncertainty of about 17% at Q^2 of 0.8 GeV^2. The error is essentially all statistical. The run exhausted only a part of the allotted time for E89-033, and the inital current and polarization from the polarized source were relatively low. Experimental systematic errors are about $\pm 2\%$. Theoretical uncertainties caused by distortions, two-body currents, and the like have also been analyzed. These results suggest that the total theoretical and experimental uncertainty in future high-statistics measurements will be small enough to provide a sensitive test of the predictions of medium-induced changes in the form factor ratio made recently by the Adelaide group [21]. The performance of the polarized source during the related measurements on the free proton in E93-027 suggests that small statistical errors will be possible with reasonable running times for nuclear targets.

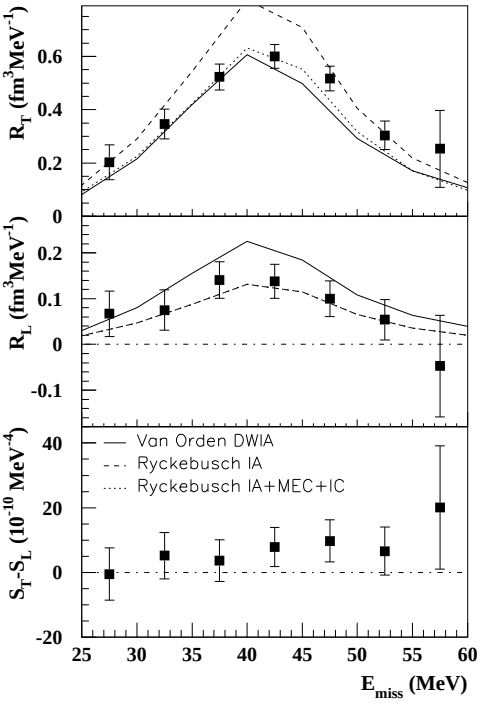

Figure 24: *The separated response functions and the difference of the longitudinal and transverse spectral functions for the* $|\theta_{pq}| = 0°$ *setting* ($\langle P_{miss} \rangle \approx$ *60 MeV/c). The calculations have been binned in the same manner as the data.*

2.3 E91-026

Measurements of the Deuteron Elastic Structure functions at Large Q^2

J. Gomez and G. G. Petratos, Spokespersons,
and
The Hall A Collaboration

JLab experiment E91-026 measured the deuteron elastic structure functions, $A(Q^2)$ and $B(Q^2)$, up to large momentum transfers. It took data for 2 months of beam time in the fall of 1997 using the JLab electron beam and the Hall A spectrometer facility. The beam energy ranged from 0.5 to 4.4 GeV and the beam current was as high as 120 μA. Incident electrons were scattered off a 15 cm liquid deuterium target cell. Elastically scattered electrons were detected in the electron high resolution spectrometer (HRSe). Recoiling deuterons were detected in coincidence in the hadron spectrometer (HRSh). Both spectrometers used two planes of scintillators for triggering and timing, and a drift chamber system for particle tracking. HRSe was also equipped with a gas Čerenkov counter and a lead-glass calorimeter for electron identification. Coincidence events were identified using time-of-flight between an electron trigger and a recoil deuteron trigger.

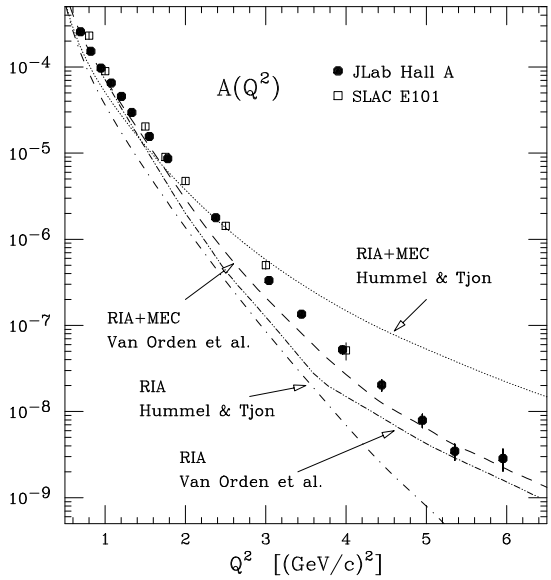

Figure 25: *The deuteron elastic structure function $A(Q^2)$ from JLab experiment E91-026 compared to RIA and RIA+MEC theoretical calculations. Also shown are previous SLAC data.*

The $A(Q^2)$ elastic structure function has been extracted in the range $0.7 < Q^2 < 6.0$ (GeV/c)^2 from cross section measurements at forward angles. Measurements of the cross section at a backward angle (144.5°) enabled separation of the $B(Q^2)$ elastic structure function by means of a Rosenbluth separation in the range $0.7 < Q^2 < 1.4$ (GeV/c)^2. A letter describing the $A(Q^2)$ results was published in Feb. 1999 [20]. Details on the experiment and references to previous data and theoretical calculations are given there.

E91-026 has significantly extended the Q^2 range of the previous $A(Q^2)$ SLAC measurements, as shown in Fig. 25, and has measured a record low cross section in electron-nucleus scattering: the average cross section for the highest Q^2 point (measured with two different beam energies) is approximately 2×10^{-41} cm^2/sr. The JLab data continue the trend of the SLAC data: they are indicative of a smooth $A(Q^2)$ fall off with Q^2 and do not exhibit any diffractive feature. The double-dot-dashed and dot-dashed curves in Fig. 25 represent the relativistic impulse approximation (RIA) calculations of Van Orden, Devine and Gross (VDG) and Hummel and Tjon (HT), respectively. The VDG curve is based on the Gross equation. The HT curve is based on a quasi-potential approximation of the Bethe-Salpeter equation. Both groups have augmented their models by including the $\rho\pi\gamma$ meson-exchange current (MEC) contribution. The magnitude of this contribution depends on the $\rho\pi\gamma$ coupling constant and vertex form factor choices. Although our data favor the VDG RIA+MEC calculation, a complete test of the RIA+MEC framework will require improved/extended measurements of the nucleon form factors and of the deuteron $B(Q^2)$.

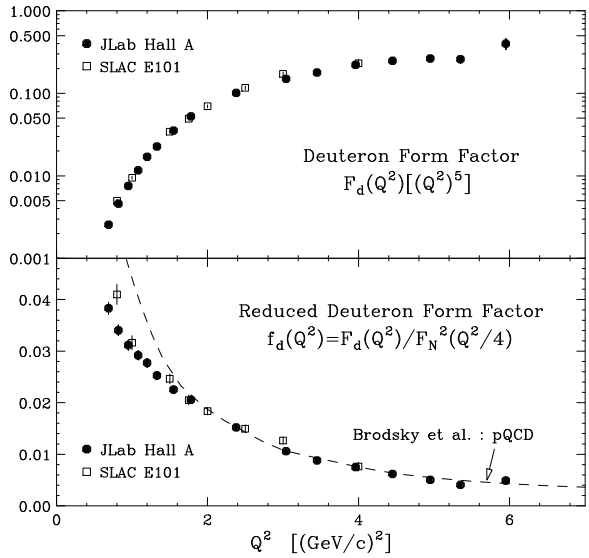

Figure 26: *The deuteron form factor $F_d(Q^2)$ times $(Q^2)^5$ (top) and the reduced deuteron form factor $f_d(Q^2)$ (bottom) from JLab E91-026 and from SLAC. The curve is the asymptotic pQCD prediction arbitrarily normalized to the data at $Q^2 = 4$ (GeV/c)^2.*

At sufficiently large Q^2 the deuteron form factors are expected to be calculable in terms of only quarks and gluons. Quark dimensional-scaling (QDS) predicts that the underlying dynamical mechanism during elastic electron-deuteron scattering is the rescattering of the constituent quarks via the exchange of hard gluons, which implies for the "deuteron form factor", $F_d(Q^2) \equiv \sqrt{A(Q^2)}$, that $F_d(Q^2) \sim (Q^2)^{-5}$. Perturbative QCD (pQCD) introduces only slowly varying logarithmic corrections with Q^2 to the QDS prediction. Fig. 26 (top) shows our measured values of $F_d(Q^2)$ multiplied by $(Q^2)^5$. It is evident that our data show an approach to a scaling behavior consistent with the power law of QDS and pQCD. Figure 26 (bottom) shows values for the "reduced" deuteron form factor $f_d(Q^2) \equiv F_d(Q^2)/F_N^2(Q^2/4)$, where the two powers of the nucleon form factor $F_N(Q^2) = (1 + Q^2/0.71)^{-2}$ remove in an approximate way the effects of nucleon compositeness. Our $f_d(Q^2)$ data appear to follow, for $Q^2 > 2$ (GeV/c)^2, the asymptotic Q^2 prediction of pQCD.

The $B(Q^2)$ data analysis is still in progress. Preliminary $B(Q^2)$ data are shown in Fig. 27. It can be seen that E91-026 has provided precise data that will put severe constraints in the parameters of the few-body "standard model" framework based on the impulse approximation and meson-exchange currents. The $B(Q^2)$ analysis is expected to conclude by the end of next month. A letter summarizing the $B(Q^2)$ results will be submitted for publication in a few months.

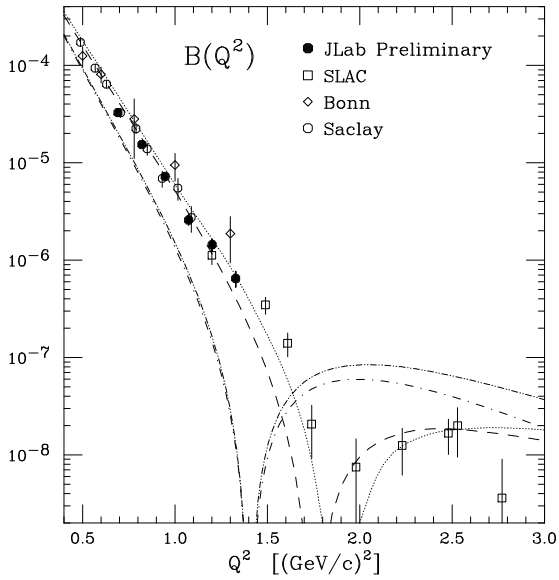

Figure 27: *JLab E91-026 preliminary results for the deuteron $B(Q^2)$ compared to RIA and RIA+MEC theoretical calculations (curves are as in Fig. 25). Also shown are previous Saclay, Bonn, and SLAC data.*

2.4 E93-027

Electric Form Factor of the Proton by Recoil Polarization

C.F. Perdrisat, M.K. Jones, V. Punjabi, Spokespersons
and
The Hall A Collaboration

This experiment received 7 weeks of beam time between May and August, 1998. The ratio G_{Ep}/G_{Mp} was measured at 8 values of Q^2, the 4-momentum squared, between 0.5 and 3.5 GeV^2. The data have been fully analyzed, and a Phys. Rev. Lett. paper has been submitted and accepted [22]. The results are also given in Table 15 below. The results can also be seen in Fig. 28. One can clearly see that above Q^2=1 GeV^2, the $\mu G_{Ep}/G_{Mp}$ ratio is falling consistently, where earlier data had been more suggestive of a constant ratio. One notices immediately that the precision of the data compared to previous measurements is much higher, particularly at $Q^2 > 1.5$ GeV^2.

The data from E93-027 have dramatically improved our knowledge of the proton electromagnetic form factors up to Q^2=3.5 GeV^2. However, it should be pointed out that precision measurements of $allfour$ elastic form factors of the nucleon are required to test theories of the strong interaction. Over the Q^2 range available at JLab, G_{Mp} is known quite well, but G_{Ep} was not until the results of JLab E93-027; the neutron form factors will be measured in other experiments at JLab in the near future.

Table 15: *The ratios $\mu_p G_{Ep}/G_{Mp}$ from this experiment.*

$< Q^2 >$	E_e	θ_p	$\mu_p G_{Ep}/G_{Mp}$	σ_{stat}	σ_{sys}
GeV^2	GeV	degrees			
0.49	0.934	45.3	0.966	0.022	0.011
0.79	0.934	30.8	0.950	0.015	0.017
1.18	1.821	40.4	0.869	0.014	0.027
1.48	3.395	46.5	0.798	0.033	0.035
1.77	3.395	42.9	0.728	0.026	0.047
1.88	4.087	43.4	0.720	0.031	0.060
2.47	4.090	37.7	0.726	0.027	0.062
2.97	4.087	33.6	0.612	0.032	0.056
3.47	4.090	29.9	0.609	0.047	0.045

We have seen an unexpected and significant difference in the Q^2 dependence of the magnetic and electric form factors of the proton. Extending the Q^2 range beyond 3.5 GeV^2 will further map the electric form factor into a transition region where subnucleonic degrees of freedom are becoming increasingly important. Indeed, at the January, 1999, Jefferson Lab PAC, a new proposal to continue the measurement of the ratio of the electric to magnetic form factors, G_{Ep}/G_{Mp}, up to a Q^2 of 5.6 GeV^2 using the recoil polarization method was approved for 28 days of running (E99-007).

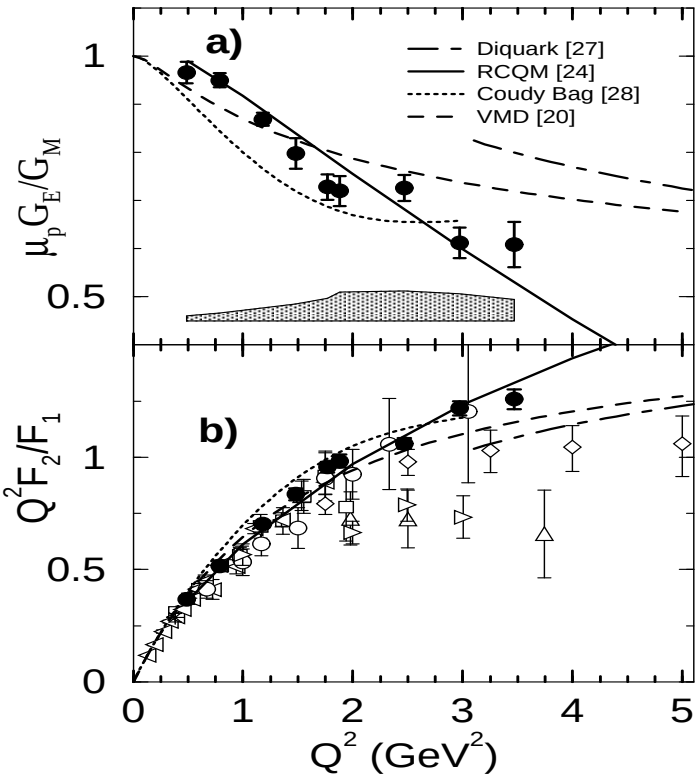

Figure 28: *(a) The ratio $\mu_p G_{Ep}/G_{Mp}$ from this experiment, compared with theoretical calculations; the absolute value of σ_{sys} is shown by the shaded area. (b) The ratio Q^2F_{2p}/F_{1p} for the same data, compared to the same theoretical models as in 3a and world data; symbols are [23](Upward Triangles),[24](Boxes),[25](Left Triangles), [26](Circles),[27](Right Triangles), [28](Diamonds), [29](Asterisks), and [30](Downward Triangles).*

2.5 E94-010

A Measurement of the Neutron (^{3}He) Spin Structure Functions at Low Q^2; a Connection Between the Bjorken and GDH Sum Rules

G.D. Cates
and
The Jefferson Lab E94-010 Collaboration

Experiment E94-010 successfully took data between September 25 and December 24, 1998. The physics goals of the experiment are summarized by the title of our original proposal: "A Measurement of the Neutron (^{3}He) Spin Structure Functions at Low Q^2; a Connection Between the BJ and GDH Sum Rules". The

experiment was designed to study spin asymmetries in the scattering of polarized electrons from a polarized ^{3}He target through a wide range of both invariant mass W and Q^2. The data provides a first glimpse of spin structure below the deep inelastic regime, and a measurement of the "extended" Gerasimov-Drell-Hearn (GDH) Sum Rule in the range $0.2 < Q^2 < 1.0$. Because the GDH sum rule makes a hard prediction for the real photon $Q^2 = 0$ point, and because the extended GDH sum rule can be related simply to the first moment of the longitudinal spin structure function $g_1(x, Q^2)$, our measurement lends itself to definite predictions in a Q^2 regime that is often considered unwieldy from a theoretical perspective. Recent results by Ji and Osborne, for instance, provide a definite framework for extending the GDH sum rule beyond the $Q^2 = 0$ point, as well as presenting a leading order result using Heavy Baryon Chiral Perturbation Theory [31]. More theoretical results appear to be forthcoming.

Technically, our experiment established several important precedents for Jefferson Laboratory. Ours was the first experiment to utilize the polarized ^{3}He target. Indeed, a great deal of our collaboration's efforts went into the construction of this target. At a length of 40 cm and a density corresponding to 10–12 atm., the polarized ^{3}He target is the thickest polarized ^{3}He target that has been used in an electron scattering experiment. Also, despite beam currents as high as 15 μA, the target polarization was maintained at 32–40% throughout most of our data taking. A more complete description of the target is contained elsewhere in Section 1.5.

Our experiment was also the first to utilize a strained GaAs cathode in the polarized electron gun. The beam polarization was roughly 70%, and availability was excellent. With beam currents that were often in the 10–15 μA range, and the high polarizations, the quality factor of the electron beam was the best that has ever been achieved in the world.

Since we were studying inclusive electron scattering, we used both the electron and hadron arms for the detection of electrons. Because we had a reasonably large pion background for some of our kinematic points, we built and commissioned for this experiment a new shower counter for use in the hadron arm. In this configuration, the rate at which we could acquire data was sometimes limited by the data acquisition system (DAQ). For this reason, a second DAQ was commissioned. When running both DAQ's simultaneously, we were able to acquire data at roughly 5K events/second.

Data were collected at six energies: 862 MeV, 1720 MeV, 2591 MeV, 3384 MeV, 4240 MeV, and 5070 MeV. We note that two new energy calibration schemes were commissioned during our experiment, one based on $e - p$ scattering, and the other based on measurements using the arc magnets that lead into the hall. Because of the wide range in W and Q^2 covered by our experiment, we used 69 separate momentum settings. All measurements were made at a scattering angle of 15.5°. The beam was in use for 1062 hours, resulting in roughly 2300 separate runs. Our data provide reasonable coverage from the quasielastic peak, through the resonance region, to the lower end of the deep inelastic regime.

While our data are voluminous, we recorded over 5 terabytes, the analysis is proceeding nicely. We have studied many issues, including scintillator efficiencies, Čerenkov efficiencies, and the spectrometer optics. In fact, we used some of our beam time to acquire the most complete set of optics data to date using 7 carbon foils. A good understanding of the spectrometer optics is important to us as we will be extracting absolute cross sections from our data. Asymmetries are generally easier to extract, and we have already presented the raw asymmetries from the first pass of our data at several conferences. The asymmetries show rich structure, with large asymmetries corresponding to the Δ, and pronounced asymmetries at higher resonances as well. We are currently working on radiative corrections, acceptance corrections (which are complicated by the large number of kinematic points), and deadtime corrections, just to name a few. The target polarization was monitored during the run using an NMR system. The NMR system, in turn, is calibrated using two techniques. One, relying on the comparison of the ^{3}He NMR signals with the NMR signals of thermally polarized water, is almost complete. A second independent calibration method relying on a comparison of ^{3}He NMR signals with electron paramagnetic resonance (EPR) signals from rubidium, is still in progress.

With work on many aspects of the analysis nearing completion, we expect to do a second pass on our data relatively soon. We expect to submit our first results for publication during the winter of 1999-2000. We note finally that five students will be receiving Ph.D.'s for work related to E94-010.

2.6 E95-001

Precise Measurement of the Transverse Asymmetry in Quasielastic $^3\vec{\mathrm{He}}(\vec{e}, e')$ and the Neutron Magnetic Form Factor

J.-O. Hansen, Jefferson Lab
and
The Jefferson Lab E95-001 collaboration

We have measured the transverse asymmetry $A_{T'}$ in $^3\vec{\mathrm{He}}(\vec{e}, e')$ quasielastic scattering with high statistical precision for Q^2-values from 0.1 to 0.6 (GeV/c)^2. The data are expected to allow extraction of the neutron magnetic form factor G_M^n with an uncertainty similar to that of recent experiments on deuterium. Data analysis is currently in progress.

2.6.1 Introduction

The precise determination of the neutron magnetic form factor, G_M^n, has been the focus of much recent experimental activity. Partly, this has been driven by the fact that accurate data on G_M^n are required for experiments designed to measure the neutron electric form factor G_E^n and for parity violation experiments that plan to extract strange nucleon form factors. Moreover, G_M^n is a fundamental quantity interesting in itself, describing the distribution of magnetism inside the neutron. Accurate knowledge of G_M^n (as well as of the other nucleon form factors) allows sensitive tests of nucleon models.

Most information on G_M^n has come from unpolarized electron scattering on deuterium (see e.g. [32]). In the past, the precision of such experiments was limited to ~20% at low Q^2 due to large subtractions and theoretical model uncertainties. Recently, however, measurements of the cross section ratio $d(e, e'n)/d(e, e'p)$ [33, 34] have provided for the first time data with uncertainties of <2% for momentum transfers Q^2 from 0.1 to 0.8 (GeV/c)^2 [34]. While this precision is excellent, the results of these experiments are not fully consistent (cf. Fig. 29), and further data are desirable to clarify the situation.

An alternative approach to a precision measurement of G_M^n is the inclusive reaction $^3\vec{\mathrm{He}}(\vec{e}, e')$ [35]. Polarized ^{3}He is a good candidate for an effective neutron target because its ground-state wave function is dominated by the S-state in which the proton spins cancel and the nuclear spin is carried by the neutron. The polarized part of the e-^{3}He cross section is thus expected to be dominated by the contribution from the neutron. Unlike $(e, e'n)$ coincidence experiments, sensitivity to the neutron responses arises directly from the physics of the target nucleus.

Compared with deuterium experiments, this technique employs a different target and relies on polarization degrees of freedom. It is thus subject to completely different systematics. In quasielastic kinematics, the spin-dependent transverse

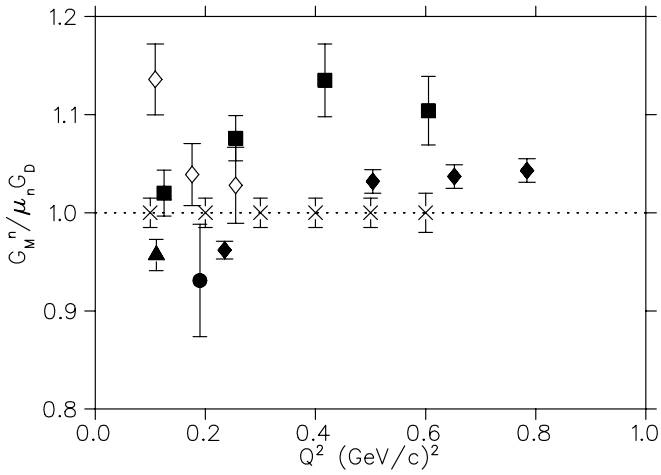

Figure 29: *The neutron magnetic form factor G_M^n in units of the standard dipole parameterization, $\mu_n G_D$, in the low Q^2 region, as determined in recent measurements: Markowitz et al. [32] (open diamonds) using $d(e,e'n)$; Bruins et al. [33] (squares) and Anklin et al. [34] (triangle and solid diamonds) using the ratio $d(e,e'n)/d(e,e'p)$; and Gao et al. [35] (circle) using $^3\vec{\mathrm{He}}(\vec{e},e')$. The expected precision of E95-001 is shown as error bars marked by crosses.*

asymmetry $A_{T'}$ [35,36] in $^3\vec{\mathrm{He}}(\vec{e},e')$ is essentially proportional to $(G_M^n)^2$, and calculations of $A_{T'}$ depend only weakly on the details of the ^{3}He nuclear ground state and the reaction mechanism, as has been shown in recent theoretical work [37–40]. Thus, a measurement of $A_{T'}$ is suitable to extract G_M^n.

2.6.2 Experiment

Experiment E95-001 was carried out in January and February 1999. $A_{T'}$ was measured for Q^2-values from 0.1 to 0.6 (GeV/c)^2 in steps of 0.1 (GeV/c)^2. A longitudinally polarized CW electron beam of 70% polarization and 10 μA cw current was incident on a high-pressure ^{3}He gas target of density 2.5×10^{20} nuclei/cm^3 polarized to $\sim$30% via spin-exchange optical pumping. The beam energies were 0.78 and 1.73 GeV. Scattered electrons were detected with the high resolution spectrometers. The elastic $^3\vec{\mathrm{He}}(\vec{e},e)$ asymmetry was continuously monitored to determine the product of beam and target polarizations with high accuracy. A total beam charge of approximately 22 C was accumulated, resulting in a total data set of 1.3×10^9 quasielastic events after background subtraction.

2.6.3 Expected Results

A statistical precision in $A_{T'}$ of better than 2.5% was achieved for each Q^2 point in a ±10 MeV bin around the center of the quasielastic peak. This precision is

better by about a factor of five that that of our previous experiment on ^{3}He [35] at $Q^2 = 0.2$ (GeV/c)^2.

For the extraction of G_M^n from the data, we will use a state-of-the-art three-body calculation that includes FSI and MEC effects. The Bochum-Krakow group [40] is currently carrying out these calculations for our kinematics. The resulting asymmetry values $A_{T'}$ as a function of G_M^n will be convoluted with the experimental acceptances, and G_M^n will be determined using a best fit of $A_{T'}(G_M^n)$ to the data in the vicinity of the quasielastic peak. Fig. 29 shows the expected precision for G_M^n.

The data also allow a detailed analysis of the dependence of $A_{T'}$ on the electron energy transfer ν. The regions away from the quasielastic peak are expected to be sensitive to details of the reaction mechanism. Thus, the shape of $A_{T'}(\nu)$ can be used to constrain calculations that include FSI and MEC corrections.

The spectrometer momentum acceptance around the elastic peak was sufficiently large to include the two-body and three-body breakup region. The resulting precision data of the ^{3}He asymmetry in this region should help refine few-body physics calculations of the ^{3}He nucleus.

Data analysis is currently in progress and results are expected in late 1999. The data will be the basis of the Ph.D. theses of W. Xu and F. Xiong (both MIT).

2.7 HAPPEX

The Hall A Parity Experiment

P. Souder, J.M. Finn, Spokespersons
and
The Hall A Collaboration

The HAPPEX experiment was divided into two runs. The first run was completed in 1998 and the results were published in 1999. [41] The measured asymmetry was consistent with A_{ns}, the value predicted in the absence of strange quarks. The goal of the second run was to increase the precision of the result by a factor of two.

During the second run, we have obtained an additional $\sim$ 80 C, doubling our total charge. However, for this data, the electrons originated from a strained GaAs crystal and were $\sim$70% polarized. The higher polarization implies that the new sample has effectively three times the statistics.

Operation with the strained GaAs crystal provided some new challenges in terms of controlling the systematic errors. First, the crystal has a large analyzing power for linearly polarized light, as high as 10%. This causes imperfections in the circular polarization of the laser light to result in large helicity-correlated intensity differences. We added a rotating half-wave plate after the Pockels cell to control the relative orientations of the relevant axes. With this modification, we were able to control this systematic successfully in the same way we did for the bulk GaAs.

A second feature of the 1999 run was that the accelerator was simultaneously delivering an intense beam to a second experimental hall. This second beam tended to have a large correlation between helicity and intensity. Moreover, there was a correlation between the position of the beam in our hall with the intensity in the second hall. To solve the problem, we modulated the intensity of the laser feeding the second hall to null the correlation. The end result is that the helicity correlations in our beam, although larger than for our 1998 data, were still small enough so that their contributions to the raw asymmetry are small compared to the statistical error.

We are presently finalizing the analysis the 1999 data. Preliminary data on the raw asymmetries as a function half-wave plate setting are given in Fig. 30. The odd data sets are expected to have the opposite asymmetry as the even sets. The data fits this pattern with a good value for the χ^2.

In addition, new data is becoming available on the electromagnetic form factors that will reduce the uncertainty in the prediction for A_{ns}. We anticipate that the final result will have an uncertainty of about half that of the published value.

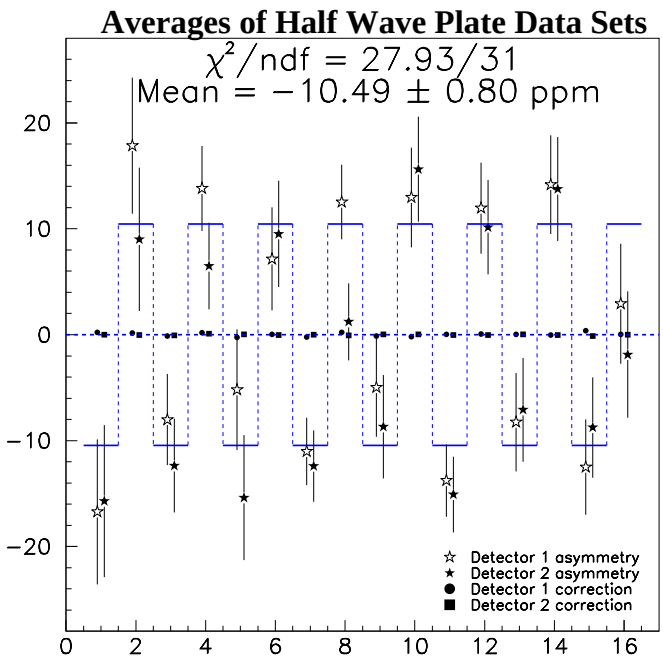

Figure 30: *Raw asymmetries for sequential data sets. Odd numbered sets have a negative sign due to the insertion of the half-wave plate.*

2.8 E89-019, E94-102, E99-008

Polarization in Two-Body Photodisintegration of the Deuteron
and
Measurement of Polarization Observables in the $p(\gamma, p)\pi^\circ$ Reaction
and
Measurement of the Angular Distribution in the $d(\gamma, p)n$ Reaction

R. Gilman, R.J. Holt, and Z.-E. Meziani, Spokespersons
and
The Hall A Collaboration

The constituent counting rules for high energy photoreactions, photopion production from the proton and two-body photodisintegration of the deuteron, appear to be approximately valid. As a test for the underlying reason for the agreement with constituent counting rules, measurements of polarization observables in deuteron photodisintegration and pion photoproduction from the proton are now in progress.

2.8.1 Status of the Experiment

Three experiments are running together to optimize the use of beam time. The three experiments [42–44] are E89-019: Polarization in Two-Body Photodisintegration of the Deuteron, E99-008: Measurement of the Angular Distribution in the $d(\gamma, p)n$ Reaction, and E94-012: Measurement of Polarization Observables in the $p(\gamma, p)\pi^\circ$ Reaction. The experiment began on August 7, 1999 and up until August 31, 1999 had received approximately two weeks of useful beam. The table below indicates the kinematics that were completed up to August 31, 1999.

Reaction	E_γ (GeV)	θ_{cm} (deg)	Quantities Measured
$\gamma p \to \pi^\circ p$	1.15	90	p_n
		120	p_n
$\gamma d \to pn$		90	p_n
$\gamma p \to \pi^\circ p$	0.86	45	p_n,C_x,C_z
		60	p_n,C_x,C_z
		75	p_n,C_x,C_z
		90	p_n,C_x,C_z
		105	p_n,C_x,C_z
		120	p_n,C_x,C_z
$\gamma d \to pn$		90	p_n,C_x,C_z
$\gamma p \to \pi^\circ p$	1.67	45	p_n,C_x,C_z
		60	p_n,C_x,C_z
		75	p_n,C_x,C_z
		90	p_n,C_x,C_z
		105	p_n,C_x,C_z
		120	p_n,C_x,C_z
$\gamma d \to pn$		90	p_n,C_x,C_z
$\gamma p \to \pi^\circ p$	4.1	75	p_n,C_x,C_z
		90	p_n,C_x,C_z
		105	p_n,C_x,C_z
		120	p_n,C_x,C_z

Only induced polarizations could be measured at 1.15 GeV because the electron beam was unpolarized. Cross sections can be extracted for all of the kinematic settings in the table. Large-angle cross sections (E99-008) for the $\gamma d \to pn$ reaction were measured at a photon energy of 1.67 GeV during this time period.

2.9 E89-028

d($\vec{e}\,e'\vec{p}$)n

P.E. Ulmer, J.M. Finn, M.K. Jones, Spokespersons
and
The Hall A Collaboration

The goal of this experiment is to provide a test of the validity of deuteron models by providing data on the recoil polarization observables in d($\vec{e}\,e'\vec{p}$)n. In addition to enhancing our understanding of the deuteron structure and reaction mechanisms in $(e, e'p)$, the information gained here will be critical in interpreting the G_E^n experiment of Madey *et al.* The Madey experiment employs an analogous reaction, d($\vec{e}\,e'\vec{n}$)p, to extract the ratio of the neutron form factors G_E^n/G_M^n, assuming that the deuteron provides a source of essentially free neutrons. Various calculations suggest that polarization transfer at quasifree kinematics is expected to be free from the effects which have frustrated extraction of form factors in Rosenbluth L/T separations, most notably final state interactions (FSI). However, the G_{En} measurement cannot test the quasifree assumption. Experiment E89-028 can test this assumption by comparing measurements on hydrogen and deuterium targets.

E89-028 ran from August 23 until August 31, 1999. E89-028 measured the recoil polarization observables of the ^{1}H($\vec{e}\,e'\vec{p}$) reaction and the ^{2}H($\vec{e}\,e'\vec{p}$) reaction in quasifree kinematics (*i.e.* centered at zero recoil momentum) at the three Q^2 points of the Madey experiment: 0.43, 1.0, and 1.61 (GeV/c)^2. The ratio of the transverse to longitudinal polarizations were measured to a statistical precision of 3%, 2% and 4.5% for the three Q^2 points, respectively. Since the Madey experiment will need to sample a fairly large range of recoil momenta (in order to achieve the required statistical precision), it is also important to test the quasifree assumption away from zero recoil momentum. Measurements were made of the three polarization components of ^{2}H($\vec{e}\,e'\vec{p}$) at $Q^2 = 1$ (GeV/c)^2 and centered at recoil momentum of 160 MeV/c which spans the range of the Madey experiment. The longitudinal and transverse components of the polarization were measured to a precision of 5%. At this recoil momentum, the measurement of the normal polarization, which is zero in the absence of FSI, will provide another constraint for this important aspect of the theory.

2.10 $K^+\vec{\Lambda}^0$

Test Measurement of $K^+\vec{\Lambda}^0$ Photoproduction at 3.3 GeV

M. Liang, A. Afanasev, K. Baker, J. Calarco, J.-P. Chen, A. Deur, R. Gilman, B. Humensky, X. Jiang, M. Jones, G. Kumbartzki, K. McCormick, S. Malov, J. Mitchell, L. Morand, C. Perdrisat, D. Prout, V. Punjabi, R. Ransome, D. Relyea, S. Strauch, L. Todor, B. Wojtsekhowski

The first polarization measurement of a photoreaction at high $-t$ was obtained from a test done in April 1999. Photo- and electro-production polarizations appear to be different. The polarizations extracted from both the entire decay cone and half of the Λ^0 decay cone are consistent with each other. Cross sections and polarizations agree reasonably well with the diquark model predications.

$K^+\Lambda^0$ photoproduction is a reaction where the induced polarization for energies above 3 GeV and $-t > 1$ (GeV/c)^2 can be studied. Since our experimental knowledge of exclusive photoreactions in this regime is extremely limited, we first proposed $K^+\vec{\Lambda}^0$ photoproduction above 3 GeV in 1998 [45]. One concern expressed by PAC14 was the use of beam time to measure the electroproduction background - the electroproduction rates are calculable, and electro- and photoproduction are expected to have the same polarizations. Also we wanted to check the technique we proposed to extract the Λ^0 polarization from half of the Λ decay cone.

A test measurement was done with the two high resolution spectrometers. The circularly polarized photon beam was produced with a 100% duty cycle, 20 μA, 3.362 GeV electron beam with 67.4% polarization hitting a 6% Cu radiator. The radiator was placed ~0.73 m upstream of the 15 cm LH_2 target. Both spectrometers were set for detecting positively charged particles: K^+ from $\gamma + p \to K^+ + \Lambda^0$ in HRSe and p from $\Lambda^0 \to \pi^- + p$ in HRSh. The test measurement was done at $\theta_K^{cm} = 90°$, which corresponds to $-t = 2.41$ (GeV/c)^2.

During the test, we found more $(\pi^+ p)$ events than anticipated. These events could not come from two-body reaction channels such as

$$\gamma + p \to \Delta^0 + p, \quad \Delta^0 \to \pi^- + p$$

or

$$\gamma + p \to \rho^0 + p, \quad \rho^0 \to \pi^+ + \pi^-$$

The phase space of these reaction channels does not fully overlap the $(K^+\Lambda^0)$ channel; rather, it may come from

$$\gamma + p \to \omega^0 + p, \quad \omega^0 \to \pi^- + \pi^+ + \pi^0,$$

where the three body decay of ω^0 can cover the phase space of the $(K^+\Lambda^0)$ reaction.

Without an aerogel detector in place during the test, singles kaons could not be separated from the large π^+ background. However, a coincidence time-of-flight resolution of 1.3ns FWHM made it possible to identify coincidence (K^+p) events, which could come either from $K^+ + \Lambda^0$ or from $K^+ + \Sigma^0$. A further cut on

reconstructed photon energy can distinguish these two channels. A Monte-Carlo simulation showed that by using $K^+ + \Lambda^0$ kinematics the end point of recontructed photon energy for $K^+ + \Sigma^0$ channel is 140 MeV lower than $K^+ + \Lambda^0$ channel. A further cut on missing mass ensures that only $K^+ + \Lambda^0$ is selected.

As the untagged bremsstrahlung beam is accompanied by electrons, the radiator measurement included both electro- and photoproduction. We also measured electroproduction only without the radiator, to find out whether we can rely on theory to calculate the electroproduction background. It is assumed that electroproduction has the same distribution as photoproduction. However, little is known experimentally, especially in the GeV range.

The c.m. kaon production cross sections, $(\frac{d\sigma}{d\Omega})_K^{cm}$, for radiator in and radiator out measurements are 3.28 ± 0.11 and 1.346 ± 0.074 (nb/sr), respectively. This results in a $K^+\Lambda^0$ photoproduction cross section of 1.93 ± 0.13 (nb/sr). The ratio of the total cross section of radiator in to radiator out is 2.44 ± 0.16, in agreement with the predicted ratio of 2.4. However, the average ratio of each setting is 3.07 ± 0.26. The difference between the average ratio and the ratio of total cross section can only be explained if the polarization of electroproduction and photoproduction is different. The $K^+\Lambda^0$ photoproduction cross section scaled by s^7 is shown in Fig. 31, together with previous measurements at 4 and 6 GeV, and with the calculation from diquark model and Non-Forward Parton Distribution (NFPD) model. The PQCD calculation is very close to the NFPD calculation. Note that even with only ~1000 counts of coincidence K^+p events, the uncertainty of these data is significantly smaller than of previous measurements.

It is surprising to see that our data at 3.3 GeV scales with 4 and 6 GeV. Carlson and Chachkhunashvili [46] observe that constituent counting rules generally work in photoreactions for photon energies above 4 GeV and $-t > 3$ (GeV/c)^2. Since we have only one data point, no definite conclusion can be drawn at this point. Our data also seem to favor the diquark model over NFPD, which probably indicates significant soft contributions in this region, beyond the hard scattering calculated in the NFPD model.

The results of our cross section measurement makes the polarization measurement even more interesting. No polarization has ever been measured in this kinematic regime. The $\overrightarrow{\Lambda^0}$ decay is self-analyzing with proton distribution in Λ^0 rest frame given by

$$(\frac{d\sigma}{d\Omega})_p = \sigma_0(1 + APcos\Theta),$$

where $A = 0.642$ is the analyzing power, P is the amplitude of Λ^0 polarization, and Θ is the angle between the out-going proton and Λ^0 polarization. There are three recoil $\overrightarrow{\Lambda^0}$ components[47]. The component normal to the reaction plane P_n results from the induced polarization: $P_n = P$, that component in the direction of

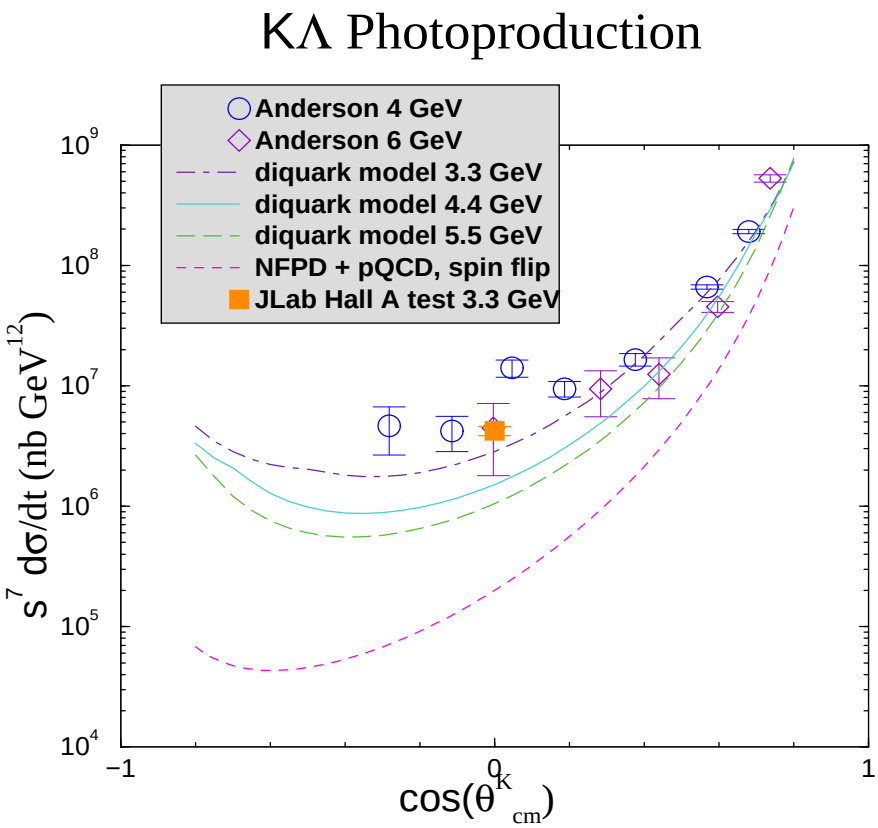

Figure 31: *Cross section for K^+ production compared to previous data and existing theories.*

the Λ^0 momentum P_l, and the in-plane component perpendicular to the direction of the Λ^0 momentum P_t are both spin transfer components that depend on the photon helicity: $P_l = hC_z$, $P_t = hC_x$, where h is the photon helicity, C_z and C_x are the longitudinal and transverse spin transfer, respectively.

Our measured polarization components are shown in Table 16. The big uncertainties in the C_x and P components are due to the poor statistics, which affected the determination of the azimuthal angle the most. Nevertheless, the difference in the polarization for radiator in and radiator out measurements is apparent. This agrees with the observation in the cross section ratio of radiator in vs. radiator out.

The polarizations extracted with data from the whole decay cone and from half of the decay cone agree within uncertainties. This will enable us in the future to measure half of the settings, which will reduce the overhead time, and at least double the statistics in each setting for the same running period.

If helicity is conserved, we expect $P = C_x = 0$. C_z varies from -1. to 1. depending on the model. If only P vanishes, it indicates amplitudes are real, whereas if only C_x vanishes, it indicates amplitudes are imaginary. No absolute

Table 16: Λ^0 *polarization measured for radiator in and radiator out runs. Results are extracted for whole and half decay cone.*

cone		Radiator in	Radiator out
whole	C_z	-0.719±0.126	-0.0075±0.216
	C_x	-0.298±0.170	-0.771±0.326
	P	-0.628±0.139	0.236±0.561
half	C_z	-0.761±0.109	0.0024±0.228
	C_x	-0.594±0.161	-0.731±0.626
	P	-0.260±0.265	0.144±0.594

conclusion on P and C_x can be drawn from the data due to the large uncertainties, especially in the radiator out measurement. Due to the limited statistics, we did not attempt to do polarization extraction for photoreaction only (radiator in - radiator out). However, the big C_z for the radiator in and small C_z for the radiator out measurement indicates that the C_z for the radiator in measurement is mostly due to the photoreaction. This result agrees well with the diquark calculation, as shown in Fig. 32.

Our test measurement has provided, for the first time, the polarization of a photoreaction at high $-t$. Both the cross section and the polarization prefers the diquark model, indicating the dominance of soft contributions in this energy regime. It will be interesting to see how this situation will change at higher energies.

The different polarizations of $K^+\Lambda^0$ electro- and photoproduction observed both in polarization and cross-section ratio indicate that we cannot only rely on the theoretical calculation of the electroproduction background. The agreement between the polarizations extracted from the whole and half of the Λ^0 decay cone confirmed the technique we proposed in [45] that by measuring only half of the decay cone one could get the same information.

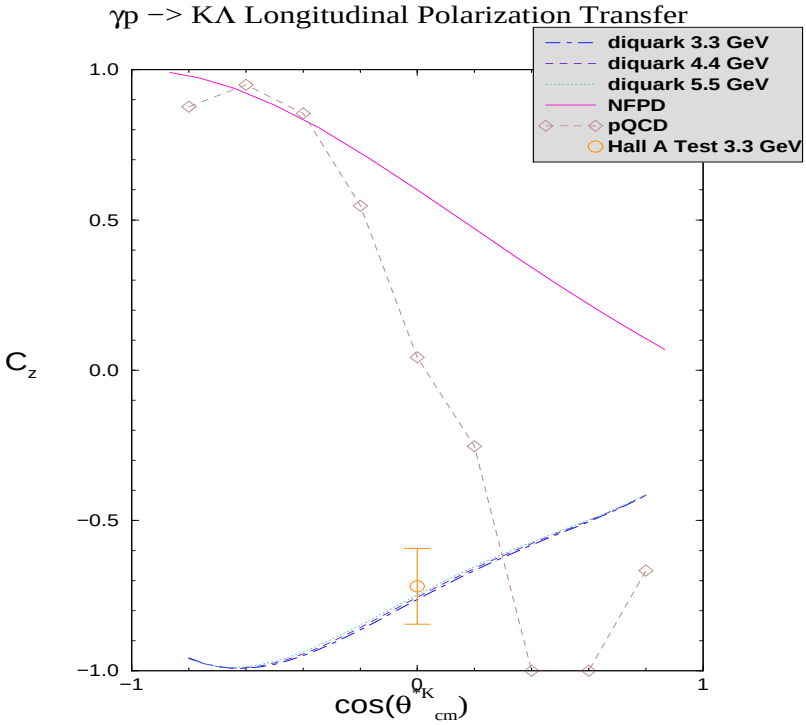

Figure 32: *Longitudinal* Λ^0 *polarization.*

2.11 E99-114

Real Compton Scattering

B. Wojtsekhowski
and
The RCS and Hall A Collaborations

Since the approval of the E97-108 proposal, Real Compton Scattering (RCS) has made great strides both in theoretical development and in the preparation for the experiment. We list below a short list of important milestones.

- Theoretical links were established between RCS, DIS, and elastic electron-proton scattering in the context of skewed parton distributions [48].
- A "proof-of-principle" for our proposed technique of using a mixed electron-photon beam with a bare photon calorimeter and veto detector was demonstrated (July 1998).
- The energy and position resolutions of the lead glass calorimeter at RCS luminosity and background was demonstrated and documented in the RCS collaboration reports of the 1998 and 1999 test runs.

- The YerPhI collaborators contributed 725 lead glass modules and PMTs for construction of the photon arm of the RCS experiment.
- Calculations of the polarization transfer were done in soft overlap approach [49] and in pQCD approach [50]. with dramatically different results.
- PAC16 approved updated RCS proposal E99-114 with A- rating and added beam time for polarization transfer measurement.
- Most of the DAQ electronics were ordered.
- Design of the lead glass-PMT assembly was completed and construction begun.
- Prototype MWPC was designed and constructed by UGa and Duke. Tests of the MWPC during July/August 1999 run show stable operation and effectiveness of the MWPC under typical RCS running conditions.
- Prototype Lucite veto detectors were built by UIUC and UNH and tested July-August 1999 run. Results show stable operation under typical RCS running conditions with excellent electron rejection. Final design of the actual detector will be completed shortly.
- The overall layout of the experiment has been finalized and a detailed design has begun.

2.11.1 Introduction

One of the primary motivations for E99-114 is to explore links among the processes of RCS and deep inelastic and elastic electron scattering from the proton. Calculations [48] using the soft overlap approach provide a theoretical framework for a description of all three processes in terms of skewed parton distributions (SPD). Using a particular model for the SPD that is highly constrained by the known parton distribution functions (DIS), he successfully account for existing RCS and form factor data. This suggests that dominance of the purely pQCD mechanism requires considerably larger s, t values than presently accessible at JLab ($\sim 5-10$ (GeV/c)^2). An important consequence of the soft overlap approach is the factorization of the RCS cross section into the Klein-Nishina (KN) cross section for scattering from a point Dirac particle (the struck quark) and a form factor $R(t)$ which contains all the important structure information:

$$d\sigma_{RCS} \; = \; d\sigma_{KN} * R^2(t) \tag{3}$$

This expression leads to the (approximate) s-independence of the ratio $d\sigma/d\sigma_{KN}$ at fixed t, a prediction which is distinctly different from that of the purely pQCD mechanism and which can be tested experimentally (see Fig. 33). $R(t)$ is similar to

but different from the Dirac form factor $F_1(t)$. In particular, in RCS the $u-$quark contribution is greatly enhanced compared to electron scattering because of the two photon vertices, thereby suggesting the use of RCS for flavor decomposition of the proton structure. Moreover, Radushkin's model for $R(t)$ leads to an effective scaling power for $d\sigma/dt(\theta_{cm})$ which is different from the asymptotic scaling law predicted by pQCD and which can also be tested experimentally (see Fig. 34).

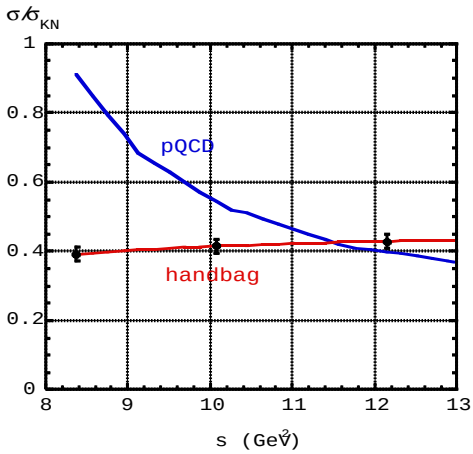

Figure 33: *Ratio of the RCS cross section to KN for $-t$=5 GeV^2 as a function of s. The points show expected data for E99-114.*

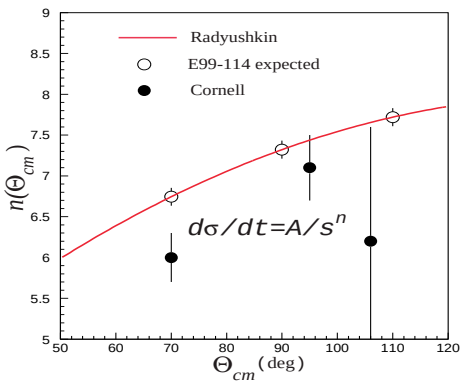

Figure 34: *Scaling of the RCS cross section as a function of θ_{cm}. The full circles are the Cornell data. The open circles represent the projected precision from our project. For the pQCD mechanism $n \equiv 6$.*

Radyushkin's work was extended [51], leading to the result:

$$d\sigma_{RCS} \; = \; d\sigma_{KN} * (f_V R_V^2(t) + (1 - f_V) R_A^2(t)) \tag{4}$$

where the additional term contributes $\sim$ 10% to the cross section at our kinematics. Diehl revealed a new formfactor R_A, accessible in polarization transfer experiments as first suggested by M.Diehl [49].

$$A_{LL} \frac{d\sigma}{d\sigma_{KN}} \; = \; f_P R_V(t) R_A(t) \tag{5}$$

Numerical results show that at large s and t $A_{LL}(\theta_{cm})$ looks qualtitatively similar to the KN result and very unlike that of the pQCD prediction, where even the sign is different (see Fig. 35). One goal of E97-114 is to test this prediction.

The proton structure is contained in the form factors, R_V and R_A, which have a simple physical interpretation. The combination $|R_V(t) + R_A(t)|^2$ is the probability that a photon can scatter elastically from the proton by transferring t to a single active quark whose helicity is oriented in the direction of the proton helicity. Similarly $|R_V(t) - R_A(t)|^2$ is the probability that the active quark has helicity opposite to that of the proton.

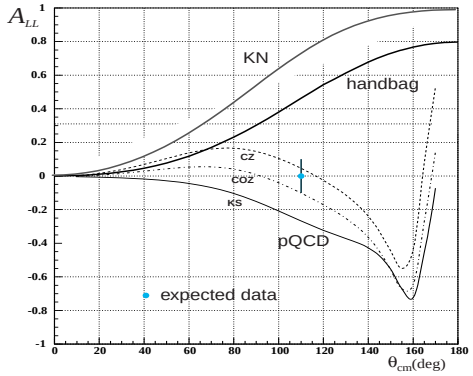

Figure 35: *Longitudinal polarization transfer parameter A_{LL} at 4 GeV. The solid curve is the prediction based on the handbag mechanism. The other curves are pQCD calculations with various DA's. The point shows the planned datum with its error bar.*

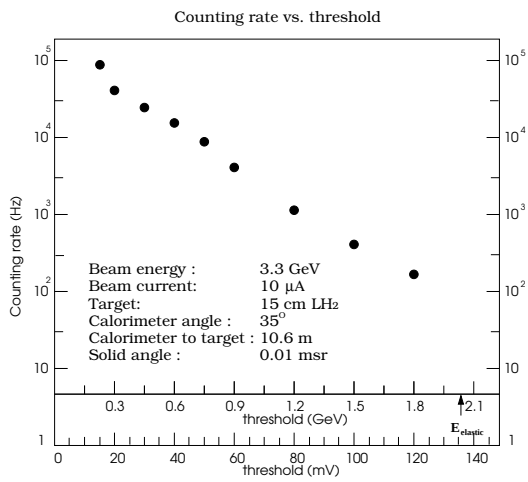

Figure 36: *Counting rate in the calorimeter at one of RCS kinematics.*

2.11.2 Proof of Mixed Beam Applicability

A crucial point of E97-114 is the high luminosity, about 300 times the luminosity of previous RCS measurement at Cornell. Test run data demonstrated a clean identification of Compton scattering. An experimental check of radiation damage of the lead glass used in the photon calorimeter under RCS radiation conditions shows a factor ~ 10 in the radiation budget before light transmission in the glass will degrade.

Fig. 36 shows the counting rate of the calorimeter at different threshold levels for one of RCS kinematics measured during the August run. At proposed threshold of 1 GeV the rate of the full scale Photon Arm is expected to be ~ 50 kHz.

The test run results are shown in Fig. 37 and Fig. 38. The data shown include endpoint runs without radiator and off-endpoint runs with the radiator. For all runs, the beam energy was 3.317 GeV and the calorimeter angle was at 35.0^o. The analysis of these data relies on the difference $\theta_\gamma^{in} - \theta_p^{in} = \Delta\theta$ (the difference of the in-plane angle from calorimeter measurement and ep kinematic prediction) and $\theta_\gamma^{out} - \theta_p^{out} = \Delta\phi$ (out-of-plane angle difference).

In Figs. 37 and 38, various cuts were applied to $\Delta\theta$ for endpoint and off-endpoint data, respectively.

Considering first the off-endpoint case, Fig. 38, the upper-left plot shows all coincidence events. The peak at the center is primarily due to ep scattering and secondarily to RCS, whereas the continuum is due to π^0 decay photons. For the middle-left plot, a cut is made requiring that the in-plane angle θ be close to that expected for two-body kinematics $-0.01 < \Delta\theta < 0.01$; this clearly enhances the

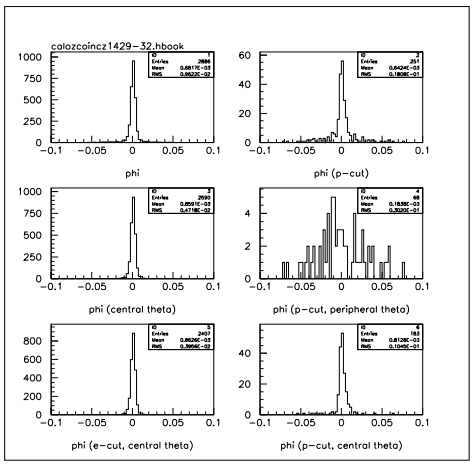

Figure 37: *Projections of the $\Delta\theta$ versus $\Delta\phi$ plot onto the $\Delta\phi$ axis for the endpoint runs. The cuts for the different panels are discussed in the text.*

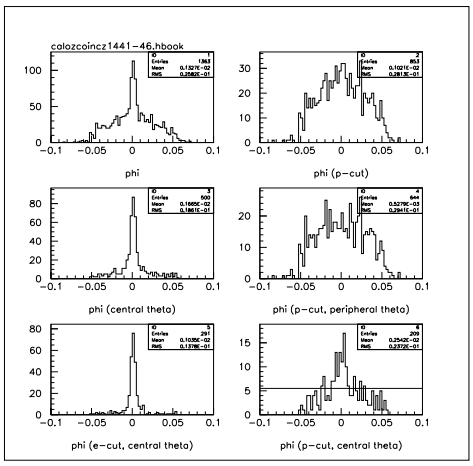

Figure 38: *Projections of the $\Delta\theta$ versus $\Delta\phi$ plot onto the $\Delta\phi$ axis for the off-endpoint runs. The cuts for the different panels are discussed in the text.*

central peak. The lower-left plot in addition requires a signal in the veto detector, therefore picking out the *ep* events.

The right plots select on the events that do not pass the veto cut; this should give only photons if the veto detector is 100% efficient. In reality there are still electrons present which we must take into account later. An anti-cut on $\Delta\theta$ (called peripheral theta) is shown in the middle-right and preferentially picks out the π^0 decay photons, whereas a *theta*-central cut (lower-right, $-0.01 < \Delta\theta < 0.01$) selectively enhances the RCS events, with some continuum mixed in.

Roughly, the events above the horizontal line in the lower-right plot represent RCS events plus the contamination of *ep* due to the inefficiency of the veto detector. To estimate the contamination, we look at the endpoint data, Fig. 37. The lower-left are the events that passes the veto and central theta cut, and therefore should be all electrons. The lower-right are the events that pass the central θ cut but failed the veto cut. These are the electrons that veto detector failed to detect. The number of events of veto-not-detected to veto-detected is $183/2407 = 0.076$. The veto efficiency is therefore $2407/(2407+183) = 93\%$. The dead time of the front end electronics is a major contributor to efficiency loss.

Now refer to Fig. 38, the lower-left plot. There are 291 events. Due to the veto-inefficiency, there will be approximately 291*0.076=22 electrons appearing on the lower-right plot. The number of events above the solid horizontal line is 49. 22 out of 49 are electrons, therefore the remaining 27 are the RCS. From the Cornell RCS cross section data we roughly estimate about 35 events (see the RCS proposal, page 33, Table 2), which is reasonable.

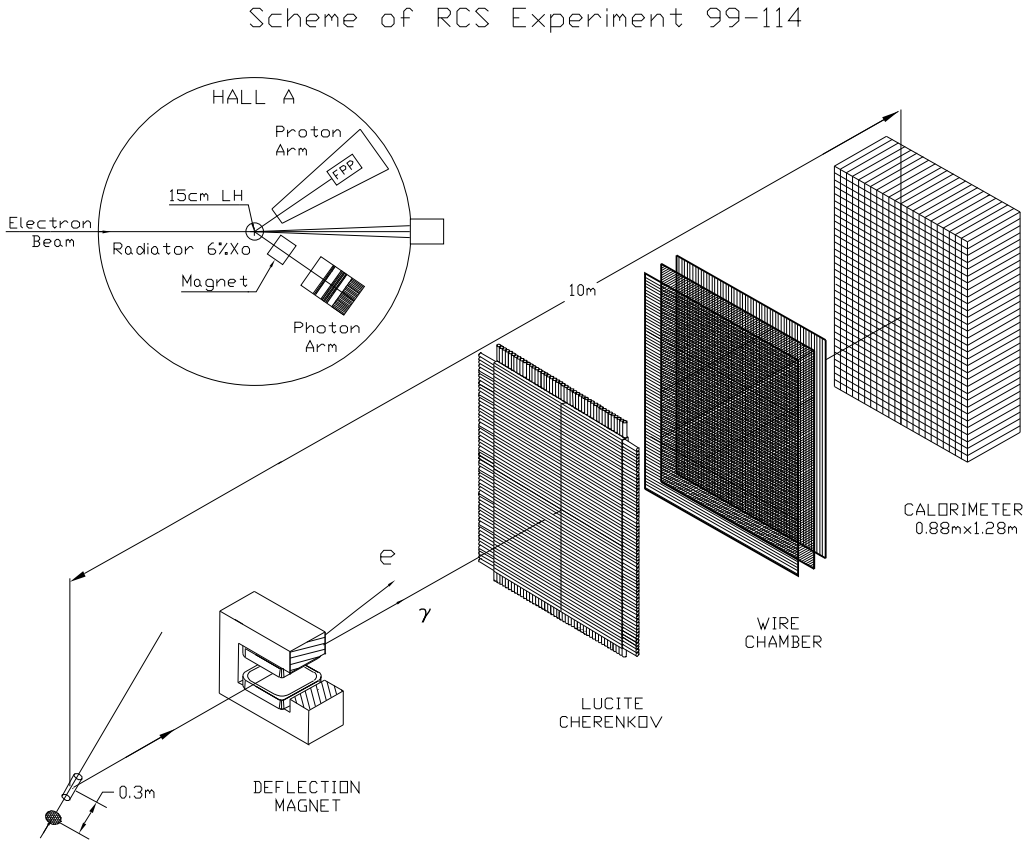

Figure 39: *Schematic view of the RCS Photon Arm detectors.*

The deflection magnet (see Fig. 39) will provide an additional tool to eliminate ep events - they will be shifted in $\Delta\theta$ correlation by 20 mrad.

2.11.3 Layout of the Experiment

The main part of DAQ electronics will be located on the service platform of the high momentum HRSe where the hadron detector package will be moved in late summer 2000. The photon calorimeter with the veto detectors will be mounted on the detector platform. The small weight of the (unshielded) detector platform allows the overhead crane to be used for repositioning for each kinematic point. A three-dimensional presentation of the layout is shown in Fig. 39.

The calorimeter consists of 32 layers, each having 22 lead glass modules. Each calorimeter module is a $40 \times 40 \times 400$ mm lead glass block of type TF–1. Light is detected by a 34-mm diameter PMT of type FEU-84-3. Each module is wrapped with one layer of an aluminized mylar and one layer of black tedlar. BC-630 optic grease is used for optical coupling between lead glass and PMT. Each PMT has

a magnetic shield. The front face of each module is open to provide for optical calibration and UV curing. A titanium flange glued to the lead glass is used for coupling the PMT housing to the lead glass block. The housing has a spring which provides a permanent load of 8 lbs along axis of the PMT. The results of calorimeter test are shown in Fig. 40 (see 1999 RCS internal report).

A standard configuration of the proton spectrometer with FPP will be used. The recently constructed S0 counter will be used to generate a fast proton signal for the coincidence logic in the photon arm DAQ. The angular resolution in the proton momentum reconstruction and accuracy of the vertex reconstruction in the target are very important parameters for indentification of Compton events. At large proton momentum, scattering in the target and HRS windows contribute only about 0.5 mrad. Moreover, the photon arm angular resolution will be better than 1 mrad. Therefore the overall angular resolution will be dominated by the intrisic optics of the HRS. Since the largest proton momentum is the maximum of the HRS dipole (~ 4.5 GeV/c), optimization and calibration of the optics will need special attention in the near future.

The extension of RCS for higher beam energy was presented at the "CEBAF at 12 GeV" workshop and the "Exclusive Reactions" workshop [52].

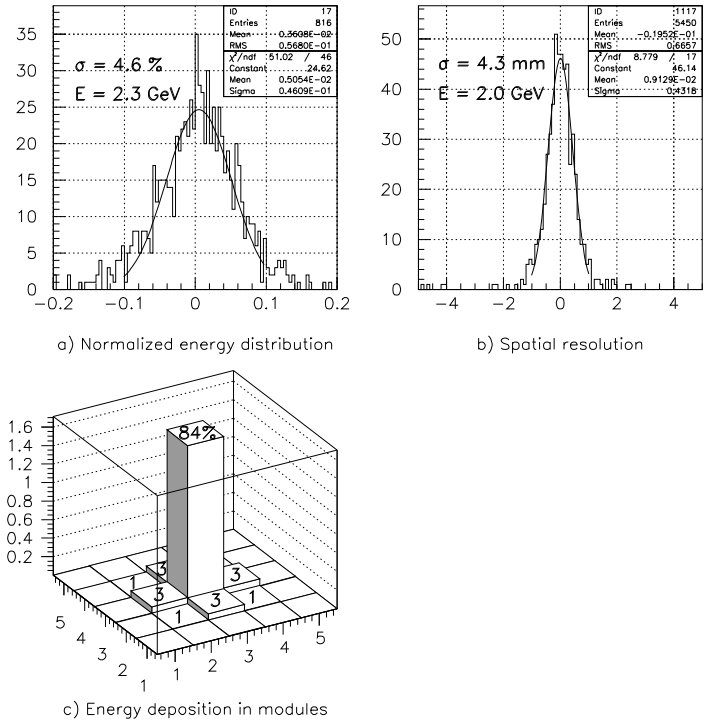

Figure 40: *Some results of shower parameters reconstruction, obtained by using calorimeter prototype* 5×5 *during test runs: a) – Normalized energy distribution, giving the energy resolution* $\sigma = 4.6\%$ *for* $2.3\ GeV$ *electron. b) – Spatial resolution, obtained from the MWPC track and reconstructed shower cluster center, is* $\sigma = 4.3\ mm$ *for* $2\ GeV$ *electron. c) – Energy deposition in adjacent modules, when* $2\ GeV$ *electron hits the center of cluster. Portions of energy deposition in each module are given in percents.*

References

[1] http://www.jlab.org/e94010/

[2] http://www.jlab.org/~incerti/technotes.html

[3] J. B. Mandeville, Ph.D. thesis, University of Illinois at Urbana-Champaign, 1993 (unpublished).

[4] René Brun and Fons Rademakers, "ROOT — An Object-Oriented Data Analysis Framework", Proceedings AIHENP'96 Workshop, Lausanne, Sep. 1996, Nucl. Inst. & Meth. in Phys. Res. **A389**, 81 (1997).

[5] The ROOT System Web site: `http://root.cern.ch`.

[6] J.Gao *et al.*, Dynamical Relativistic Effects Observed in Quasielastic **1p**−Shell Proton Knockout from ^{16}O, submitted to Phys. Rev. Lett.

[7] N. Liyanage *et al.*, A study of the ^{16}O(e,e$'$p) reaction at deep missing energies, in preparation.

[8] F. Garibaldi *et al.*, Nucl. Instrum. Methods **A314,** 1 (1992).

[9] G.G. Simon *et al.*, Nucl. Phys. **A333**, 381 (1980).

[10] J.M. Udias *et al.*, LANL Preprint Library, nucl-th/9905030.

[11] J.J. Kelly, LANL Preprint Library, nucl-th/9905024.

[12] J.J. Kelly, Adv. Nucl. Phys. **23**, ed. by J.W. Negele and E. Vogt, 75 (1996).

[13] J. Ryckebusch *et al.*, Nucl. Phys. **A476**, 237 (1988).

[14] J. Ryckebusch *et al.*, Nucl. Phys. **A503**, 694 (1989).

[15] V. Van der Sluys, K. Heyde, J. Ryckebusch, M. Waroquier, Phys. Rev. **C55** 1982 (1997).

[16] J. Ryckebusch *et al.*, Nucl. Phys. **A624**, 581 (1997).

[17] J.P. Jeukenne and C. Mahaux, Nucl. Phys. **A394**, 445 (1983).

[18] P.E. Ulmer *et al.*, Phys. Rev. Lett. **59**, 2259 (1987).

[19] D. Dutta, Ph.D. thesis, Northwestern University, 1999 (unpublished).

[20] L. C. Alexa *et al.*, Phys. Rev. Lett. **82**, 1374 (1999).

[21] D.H. Lu *et al.*, Phys. Lett. B **417**, 217 (1998).

[22] http://www.jlab.org/j̃ones/gep/gepprl.ps

[23] J. Litt *et al.*, Phys. Lett. B **31**, 40 (1970).

[24] Ch. Berger *et al.*, Phys. Lett. B **35**, 87 (1971).

[25] L.E. Price *et al.*, Phys. Rev. D **4**, 45 (1971).

[26] W. Bartel *et al.*, Nuc. Phys. B **58**, 429 (1973).

[27] R.C. Walker *et al.*, Phys. Rev. D **49**, 5671 (1994); R.C. Walker *et al.*, Phys. Lett. B **224**, 353 (1989).

[28] L. Andivahis *et al.*, Phys. Rev. D **50**, 5491 (1994); P.E. Bosted *et al.*, Phys. Rev. Lett. **68**, 3841 (1992).

[29] B. Milbrath *et al.*, Phys. Rev. Lett. **80**, 452 (1998); erratum, Phys. Rev. Lett. **82**, 2221 (1999).

[30] R. Arnold *et al.*, Phys. Rev. Lett. **57**, 174 (1986); A.F. Sill *et al.*, Phys. Rev. D **48**, 29 (1993).

[31] Xiangdong Ji and Jonathan Osborne, hep-ph/9905410.

[32] P. Markowitz *et al.*, Phys. Rev. **C48**, R5 (1993).

[33] E. E. W. Bruins *et al.*, Phys. Rev. Lett. **75**, 21 (1995).

[34] H. Anklin *et al.*, Phys. Lett. **B336**, 313 (1994); **B428**, 248 (1998).

[35] H. Gao *et al.*, Phys. Rev. **C50**, R546 (1994).

[36] T. W. Donnelly and A. S. Raskin, Ann. Phys. (N.Y.) **169**, 247 (1986).

[37] R.-W. Schulze and P. U. Sauer, Phys. Rev. **C48**, 38 (1993).

[38] C. Ciofi degli Atti, E. Pace and G. Salmè, Phys. Rev. **C51**, 1108 (1995).

[39] S. Ishikawa *et al.*, Phys. Rev. **C57**, 39 (1998); and private communication.

[40] J. Golak, private communication.

[41] K.A. Aniol *et al.*, Phys. Rev. Lett. 82 (1999) 1096.

[42] Jefferson Lab Exp. 89-019, R. Gilman, R. Holt, Z.-E. Meziani *et al.*

[43] Jefferson Lab Exp. 99-008, R. Gilman, R. Holt, Z.-E. Meziani *et al.*

[44] Jefferson Lab Exp. 94-012, R. Gilman, R. Holt, *et al.*

[45] M. Liang, R. Gilman, A. Afanasev, et al., Jefferson Lab PR98-106, PR99-116

[46] C.E. Carlson and M. Chachkhunashvili, Phys. Rev. **D45**, 2555 (1992).

[47] I.S. Barker, A. Connachie, and J.K. Storrow, Nucl. Phys. **B95**, 347 (1975).

[48] A.Radyushkin, hep-ph/9803316.

[49] M.Diehl et al., hep-ph/9903268.

[50] Vanderhaeghen, Nucl. Phys. **A622**, 144c, 1997.

[51] M.Diehl et al., hep-ph/9811253.

[52] A.Nathan, hep-ph/9807397/ and hep-ph/9908522/.

3 Members of the Hall A Collaboration

Bryon Anderson	Kent State University
Konrad A. Aniol	California State University, Los Angeles
David S. Armstrong	College of William and Mary
Todd Averett	College of William and Mary
F. Todd Baker	College of William and Mary
Maud Baylac	Dapnia/SPhN Orme des Merisiers CEN Saclay
Elizabeth Beise	University of Maryland
J. Berthot	Laboratoire de Physique Corpusculaire Université Blaise Pascal
Pierre Bertin	Laboratoire de Physique Corpusculaire Université Blaise Pascal
Bill Bertozzi	MIT
Louis Bimbot	Institut de Physique Nucleaire, Orsay
Tim Black	MIT
Werner Boeglin	Florida International University
Edward J. Brash	University of Regina
Vincent Breton	Laboratoire de Physique Corpusculaire Université Blaise Pascal
Herbert Breuer	University of Maryland
David Brown	University of Maryland
Etienne Burtin	Dapnia/SPhN - Orme des Merisiers CEN Saclay
John Calarco	University of New Hampshire
Larry Cardman	Jefferson Lab
Gordon D. Cates	Princeton University
Christian Cavata	Dapnia/SPhN - Orme des Merisiers CEN Saclay
Zhengwei Chai	MIT
George Chang	University of Maryland
Nicholas Chant	University of Maryland
Jian-Ping Chen	Jefferson Lab
Seonho Choi	Temple University
Eugene Chudakov	Jefferson Lab
Steve Churchwell	Duke University
Evaristo Cisbani	INFN/Sezione Sanita
Nathalie Colombel	Dapnia/SPhN Orme des Merisiers CEN Saclay
Marius Coman	Florida International University
Dan Dale	University of Kentucky
Natalie Degrande	Gent State University
Kees de Jager	Jefferson Lab
Raffaele De Leo	INFN Sezione de Lecce
Alexandre Deur	Jefferson Lab
Nicole d'Hose	Dapnia/SPhN Orme des Merisiers CEN Saclay
Sonja Dieterich	Rutgers University
Rachele di Salvo	Laboratoire de Physique Corpusculaire Université Blaise Pascal

Pibero Djawotho	College of William & Mary
Jean-Eric Ducret	Dapnia/SPhN Orme des Merisiers CEN Saclay
Dipangkar Dutta	MIT
Kim Egiyan	Yerevan Physics Institute
Martin B. Epstein	California State University, Los Angeles
Stephanie Escoffier	Dapnia/SPhN Orme des Merisiers CEN Saclay
Mike Finn	College of William and Mary
Kevin Fissum	University of Lund
Helene Fonvieille	Laboratoire de Physique Corpusculaire Université Blaise Pascal
Bernard Frois	Dapnia/SPhN CEN Saclay
Salvatore Frullani	Istituto Superiore di Sanita INFN/Sezione Sanita
Haiyan Gao	MIT
Franco Garibaldi	INFN/Sezione Sanita Istituto Superiore di Sanita
Ashot Gasparian	Hampton University
Olivier Gayou	College of William & Mary
Shalev Gilad	MIT
Ron Gilman	Rutgers University
Alexander Glamazdin	Kharkov Institute of Phy. and Tech.
Charles Glashausser	Rutgers University
Javier Gomez	Jefferson Lab
Victor Gorbenko	Kharkov Institute of Phy. and Tech.
Tim Gorringe	University of Kentucky
Keith Griffioen	College of William and Mary
Ole Hansen	Jefferson Lab
Bill Hersman	University of New Hampshire
Richard Holmes	Syracuse University
Harry Holmgren	University of Maryland
Maurik Holtrop	University of New Hampshire
Edik Hovhannisyan	Yerevan Physics Institute
Calvin Howell	Duke University
Garth Huber	University of Regina
Charles Hyde-Wright	Old Dominion University
Sebastian Incerti	Temple University
Mauro Iodice	INFN/Sezione Sanita Istituto Superiore di Sanita
Riccardo Iommi	INFN/Sezione Sanita Istituto Superiore di Sanita
Stephanie Jaminion	Laboratoire de Physique Corpusculaire Université Blaise Pascal
Johann Jardillier	Saclay Dapnia/SPhN Orme des Merisiers CEN Saclay
Steffen Jensen	Cal Tech
Xiangdong Jiang	Rutgers University
Cathleen Jones	Cal Tech
Mark K. Jones	College of William and Mary

Christophe Jutier	Laboratoire de Physique Corpusculaire Université Blaise Pascal
William Kahl	Syracuse University
Seigo Kato	Yamagata University
Mina Katramatou	Kent State University
James Kelly	University of Maryland
Sophie Kerhoas	Dapnia/SPhN Orme des Merisiers CEN Saclay
Armen Ketikyan	Yerevan Physics Institute
Kouichi Kino	Tohoku University
Ioannis Kominis	Princeton University
Wolfgang Korsch	University of Kentucky
Serge Kox	ISN Grenoble
Kevin Kramer	College of William & Mary
Laird Kramer	Florida International University
Krishna S. Kumar	Princeton University
Gerfried Kumbartzki	Rutgers University
Michael Kuss	Jefferson Lab
Geraud Lavessiere	Laboratoire de Physique Corpusculaire Université Blaise Pascal
John LeRose	Jefferson Lab
Mark Leuschner	University of New Hampshire
David Lhuillier	Dapnia/SPhN Orme des Merisiers CEN Saclay
Meihua (Meme) Liang	Jefferson Lab
Richard Lindgren	University of Virginia
Nilanga Liyange	Jefferson Lab
George Lolos	University of Regina
Robert Lourie	Renaissance Tech
Richard Madey	Kent State University
Kazushige Maeda	Tohoku University
Sergey Malov	Rutgers University
Mark Manley	Kent State University
Demetrius J. Margaziotis	California State University, Los Angeles
Pete Markowitz	Florida International University
Jacques Marroncle	Dapnia/SPhN Orme des Merisiers CEN Saclay
Jacques Martino	Dapnia/SPhN Orme des Merisiers CEN Saclay
Samvel Mayilyan	Yerevan Physics Institute
Kathy McCormick	Jefferson Lab
David Meekins	Florida State University
Zein-Eddine Meziani	Temple University
Bob Michaels	Jefferson Lab
Wilson Miller	Princeton University
Jospeh Mitchell	Jefferson Lab
Jean Mougey	ISN Grenoble
Sirish Nanda	Jefferson Lab

Alan Nathan	Univ. of Illinois
Damien Neyret	Dapnia/SPhN Orme des Merisiers CEN Saclay
Roman Pomatsalyuk	Kharkov Institute of Phy. and Tech.
Zisis Papandreou	University of Regina
Charles Perdrisat	College of William and Mary
Gerassimos G. Petratos	Kent State University
Artush Petrosyan	Yerevan Physics Institute
Stephane Platchkov	Dapnia/SPhN Orme des Merisiers CEN Saclay
Vina Punjabi	Norfolk State University
Thierry Pussieux	Dapnia/SPhN Orme des Merisiers CEN Saclay
Gilles Quemener	College of William and Mary
Ronald D. Ransome	Rutgers University
Brian Raue	Florida International University
Juerg Reinhold	Florida International University
Yves Roblin	Laboratoire de Physique Corpusculaire Université Blaise Pascal
Rikki Roche	Florida State University
Mike Roedelbronn	University of Illinois
Oscar Rondon	University of Virginia
Philip Roos	University of Maryland
David Rowntree	MIT
Gary Rutledge	College of William and Mary
Paul Rutt	Jefferson Lab
Marat Rvachev	MIT
Franck Sabatie	Old Dominion University
Arun Saha	Jefferson Lab
Teijiro Saito	Tohoku University
Adam Sarty	Florida State University
Albert Shahinyan	Yerevan Physics Institute
Karl Slifer	Temple University
Timothy Smith	University of New Hampshire
Pavel Sorokin	Kharkov State University
Paul A. Souder	Syracuse University
Steffen Strauch	Rutgers University
Riad Suleiman	Kent State University
Jeff Templon	Univ. of Georgia
Tatsuo Terasawa	Tohoku University
Luminita Todor	Old Dominion University
H. Tsubota	Tohoku University
Hiroaki Ueno	Yamagata University
Paul E. Ulmer	Old Dominion University
Guido Urciuoli	INFN/Sezione Sanita Istituto Superiore di Sanita
Luc Van de Hoorebeke	Gent State University

Robert Van de Vyver	Gent State University
Pascal Vernin	Dapnia/SPhN Orme des Merisiers CEN Saclay
Branislav (Branko) Vlahovic	North Carolina Central University
Hakob Voskanyan	Yerevan Physics Institute
Eric Voutier	ISN Grenoble
Richard Walter	Duke University
John Watson	Kent State University
Larry Weinstein	Old Dominion University
Richard Wilson	Harvard University.
Krishni Wijesooriya	College of William and Mary
Bogdan Wojtsekhowski	Jefferson Lab
Hong Xiang	MIT
Feng Xiong	MIT
Wang Xu	MIT
Valdis Zeps	University of Kentucky
Jianguo Zhao	MIT
Zilu Zhou	MIT